A 2-dimentional contact analysis using second-order virtual element method

AUTHOR(S):

Shen, Wei; Ohsaki, Makoto; Zhang, Jingyao

CITATION:

Shen, Wei ...[et al]. A 2-dimentional contact analysis using second-order virtual element method. Computational Mechanics 2022, 70(2): 225-245

ISSUE DATE:

2022-08

URL:

http://hdl.handle.net/2433/279379

Submitted to Computational Mechanics

A 2-dimentional contact analysis using second-order virtual element method

Wei Shen[1], Makoto Ohsaki[1] and Jingyao Zhang[1]

1 Department of Architecture and Architectural Engineering, Graduate School of Engineering, Kyoto University Kyoto-Daigaku Katsura, Nishikyo, Kyoto 615-8540, Japan

Abstract:

In the present study, we exploit the use of second-order virtual element method (VEM) for contact analysis in 2-dimension within the context of linear elasticity and small deformation. By virtue of mesh flexibility in the VEM, the non-matching meshes at the contact interface are transformed into matching meshes, and therefore the node-to-node contact discretization can be constructed. The frictional contact is considered as stick condition, and no tangential movement is allowed due to the assumption of small deformation condition. The normal and frictional contact constraints are imposed using the Lagrange multiplier method and the penalty method, respectively, and the candidate contact interface is determined by a series of adaptive trial and error tests as well as prior experience. Several numerical examples are investigated to illustrate the effectiveness of the proposed method in contact analysis, and the results show that the proposed method is able to handle problem with complex non-matching meshes at contact interface. Properties of shear wall consisting of units with fitting joints are also investigated as a practical application.

Keywords:

Virtual element method (VEM); Node-to-node contact; Non-matching mesh; Arbitrary polygonal element; Small deformation;

1. Introduction

Contact analysis is one of the important topics in computational mechanics, since in practical engineering the contact phenomena are inevitable for evaluating the mechanical properties of structures as assemblage of deformable or rigid substructures connected through contact surfaces. Therefore, enormous works have been carried out by researchers on the development of contact

analysis; see the review article [1] and textbook [2] for an overview of existing researches. Many methods have been proposed for solving academic problems and for industrial applications, such as interlocking assemblies of multiple rigid components [3], topology optimization of multicomponent structures with contact [4, 5] and power transfers between gears [6].

Generally, the contact analysis is considered as a constrained optimization problem, where the total potential energy of the whole mechanical system is to be minimized under the contact constraints. The problem can be solved by many different numerical methods such as the well-established Lagrange multiplier method and penalty method [2, 7]. One of the challenges in the numerical methods for contact analysis is the discretization of contact interface to handle non-matching meshes, in which some or all coordinates of nodes of the two substructures at the contact interface are not the same. For this case, the conventional node-to-node discretization scheme cannot be applied [8]. To circumvent this difficulty, the node-to-segment (or node-to-surface for 3-dimention) scheme was proposed by Hughes et al. [9] utilizing the collocation approach such that nodes on the slave side must not penetrate their opposing master side segments. However, this scheme is inherently biased and does not pass the contact patch test [10, 11]. On the other hand, the segment-to-segment (or surface-to-surface for 3-dimensional structure) scheme [10] projects the segment on one side of the contact interface onto an adjacent segment of the opposing side, and the contact virtual work is integrated along the contact interface using numerical quadrature with interpolated contact pressure. In this way the contact constraints are continuously interpolated along the contact interface even for the case of the non-matching meshes. A commonly used discretization scheme of this type is the mortar method [12] which integrates the contact virtual work on a virtual mortar domain. However, the additional discretization of non-matching meshes enhances complexity of the contact problem [2].

By contrast, due to the simplicity of the node-to-node discretization scheme [2], novel methods have been proposed in the past 20 years for converting the non-matching meshes to matching ones. The main idea behind these methods is to allow arbitrary insertion of nodes on the contact interface such that the node-to-node discretization scheme can be used to formulate contact constraints. Bitencourt et al. [13] proposed a coupling finite element (CFE) method for non-matching meshes; however, for each CFE only one extra node can be added at the element edge coinciding with the contact interface. Based on the scaled boundary finite element method (SB-FEM), which allows arbitrary discretization on element edge, Xing et al. [14][15] converted the non-matching meshes at the contact interface to matched node-to-node by inserting new nodes on the edge of corresponding elements. However, since the SB-FEM relies on defining a scaled center for each element and need to satisfy the scaling requirements, the element shape cannot be highly irregular [16].

To construct a more flexible node-to-node scheme with fewer requirements on the element shape, Wriggers et al. [17] proposed a method to model node-to-node contact constraints by making use of the arbitrary node property of virtual element method (VEM), which is a numerical discretization technique in Galerkin framework originally inspired by the mimic finite difference (MFD) method [18]. Since it is recently introduced by Beirão da Veiga [19], VEM has been extensively developed and is now applied to a wide range of engineering problems,

including linear elasticity problem with small and finite deformations [20–23], contact problem [17], fracture problem [16, 24] and structural topology optimization [25]. The main idea of VEM is that the space of local shape functions of each element is defined implicitly and projected to a polynomial space with prescribed order to approximate the element strain energy. In this way VEM avoids the explicit construction of local shape function and its integral over the element domain; and thus VEM is able to handle arbitrary polygonal mesh.

Inspired by the work by Wriggers et al. [17], the present study explores a second-order VEM formulation for 2-dimensional contact problem of linear elastic bodies with small deformation. The shape of the virtual element can be any kind of polygon, even irregular and/or concave, providing an alternative to dealing with complex contact interface. The normal contact constraint is imposed using Lagrange multiplier method, while the frictional contact (or tangential contact) constraint is assumed to be stick condition and is imposed using the penalty method. The node-to-node contact pair is constructed for each node at the contact interface, and a series of trial and error test as well as prior experience is utilized to detect the contact/separation at each node pair along the contact boundary.

One of the purposes of this paper is to investigate the properties of a shear wall attached to a building frame resisting the story shear force. Although details are not explained here, the construction cost is significantly reduced if the wall is attached to the beams and columns by contact rather than by welding or anchoring. Fukushima et al. [26] and Kimura et al. [27] proposed methods for optimizing the shape and topology of the blocks of the shear walls to be connected by contact. However, they have straight contact lines; therefore, the load transmission property is not efficient. To enhance the stiffness of the wall by contact between the units, fitting joints, also called matching or engaging joints, can be effectively used as commonly utilized for timber structures [28]. Therefore, in the numerical examples, we investigate the load carrying properties of a shear wall consisting of irregular-shaped units connected by contact at fitting joints. It is shown that the contact behavior can be successfully simulated using the second-order VEM.

The rest of the paper is organized as follows. Section 2 gives a brief introduction of second-order VEM including the basic concept and general formulation, whereas the detailed calculations of related matrices are presented in Appendix. Section 3 summaries the contact kinematics and formulates the node-to-node contact schemes for non-matching meshes by inserting nodes. Four numerical examples are investigated in Section 4 to illustrate the capability and performance of the proposed method, and finally some conclusions are drawn in Section 5.

2. Virtual element method for elasticity problem

In this section the basic concept and formulation of second-order VEM are briefly discussed, and the details of corresponding implementation are given in Appendix.

2.1 Problem statement

Consider a standard linear elasticity boundary value problem on a continuous 2-dimensional domain $\boldsymbol{\Omega} \in \mathbb{R}^2$ with boundary denoted as $\partial\boldsymbol{\Omega}$, which can be decomposed into disjoint segments $\partial\boldsymbol{\Omega}_u$ and $\partial\boldsymbol{\Omega}_t$ subjected to Dirichlet and Neumann boundary conditions, respectively. For simplicity, we assume the homogeneous boundary condition for $\partial\boldsymbol{\Omega}_u$, i.e., the displacement at $\partial\boldsymbol{\Omega}_u$ is fixed to 0, and a traction force $\boldsymbol{t}$ is applied on $\partial\boldsymbol{\Omega}_t$ whereas the body force within the domain $\boldsymbol{\Omega}$ is assumed to be zero. The variational formulation (weak form) of the standard boundary value problem is described as: find the displacement vector $\boldsymbol{u} \in H_0^1(\boldsymbol{\Omega}) \times H_0^1(\boldsymbol{\Omega})$ such that

$$a(\boldsymbol{u},\boldsymbol{v}) = f(\boldsymbol{v}),\ \forall \boldsymbol{v} \in H_0^1(\boldsymbol{\Omega}) \times H_0^1(\boldsymbol{\Omega}) \tag{1}$$

where $\boldsymbol{u} = \left[u_x, u_y\right]$ and $\boldsymbol{v} = \left[v_x, v_y\right]$ are the vector-valued functions belonging to the admissible displacement space $H_0^1(\boldsymbol{\Omega}) \times H_0^1(\boldsymbol{\Omega})$, and $H_0^1(\boldsymbol{\Omega})$ is the Sobolev space consisting of functions whose values are zero on the boundary $\partial\boldsymbol{\Omega}_u$ and the first weak derivative is square-integrable on $\boldsymbol{\Omega}$; a and f are the bilinear and linear forms, respectively, given as follows:

$$a(\boldsymbol{u},\boldsymbol{v}) = \int_{\boldsymbol{\Omega}} \boldsymbol{\sigma}(\boldsymbol{u}) : \boldsymbol{\varepsilon}(\boldsymbol{v}) d\boldsymbol{\Omega} \tag{2}$$

$$f(\boldsymbol{v}) = \int_{\partial\boldsymbol{\Omega}_t} \boldsymbol{v} \cdot \boldsymbol{t} d\partial\boldsymbol{\Omega}_t \tag{3}$$

Here in Eq. (2) the strain tensor is derived from the strain-displacement relation $\boldsymbol{\varepsilon}(\boldsymbol{u}) = \frac{1}{2}\left(\nabla\boldsymbol{u} + \nabla^T\boldsymbol{u}\right)$ in which ∇ is the gradient operator, and the stress tensor is derived from the linear elastic constitutive relation $\boldsymbol{\sigma} = \mathbb{C}\boldsymbol{\varepsilon}$ where $\mathbb{C}$ is the elasticity tensor. $\boldsymbol{\varepsilon\sigma}$

2.2 Second-order VEM formulation

Suppose the domain $\boldsymbol{\Omega}$ is partitioned into disjoint non-overlapping polygonal mesh T_h with maximum diameter h as defined in Da Veiga et al. [29], and denote the local space of any function of $H_0^1(\boldsymbol{\Omega})$ for element $K \in T_h$ as $V(K) = H_0^1(\boldsymbol{\Omega}) \cap H^1(\boldsymbol{\Omega}^K)$ where $\boldsymbol{\Omega}^K$ is the domain of element K and $H^1(\boldsymbol{\Omega}^K)$ represents the Sobolev space whose first weak derivative is square-integrable on $\boldsymbol{\Omega}^K$. Then Eq. (1) can be rewritten as

$$a(\boldsymbol{u},\boldsymbol{v}) = \sum_{K \in T_h} a^K\left(\boldsymbol{u}\big|_K, \boldsymbol{v}\big|_K\right) = \sum_{K \in T_h} f^K\left(\boldsymbol{v}\big|_K\right) = f(\boldsymbol{v}),\ \forall \boldsymbol{v}\big|_K \in V(K) \times V(K) \tag{4}$$

where $\boldsymbol{u}\big|_K$ and $\boldsymbol{v}\big|_K$ are the functions in $H_0^1(\boldsymbol{\Omega}) \times H_0^1(\boldsymbol{\Omega})$ restricted to the domain of element K, and the bilinear form a^K and linear form f^K are defined in element K as

$$a^K\left(\boldsymbol{u}|_K,\boldsymbol{v}|_K\right)=\int_{\boldsymbol{\Omega}^K}\boldsymbol{\sigma}\left(\boldsymbol{u}|_K\right):\boldsymbol{\varepsilon}\left(\boldsymbol{v}|_K\right)d\boldsymbol{\Omega}^K \tag{5}$$

$$f^K\left(\boldsymbol{v}|_K\right)=\int_{\partial\boldsymbol{\Omega}_t^K}\boldsymbol{v}|_K\cdot\boldsymbol{t}d\partial\boldsymbol{\Omega}_t^K \tag{6}$$

In Eq. (6), $\partial\boldsymbol{\Omega}_t^K$ is the boundary of element K subjected to Neumann boundary condition. For simplicity we write $a^K\left(\boldsymbol{u},\boldsymbol{v}\right)$ and $f^K\left(\boldsymbol{v}\right)$ instead of $a^K\left(\boldsymbol{u}|_K,\boldsymbol{v}|_K\right)$ and $f^K\left(\boldsymbol{v}|_K\right)$, respectively, for the rest of the paper. Without loss of generality, one element K with n vertices and n edges is used to derive the construction of second-order VEM.

In second-order VEM, the Galerkin scheme of Eqs. (5) and (6) are obtained by constructing a local virtual element space $V_h\subseteq V\left(K\right)$ of element K with second-order interpolation, and the vector-valued function $\boldsymbol{v}_h$ in the space $V_h\times V_h$ has the following properties [19]:

- $\boldsymbol{v}_h$ is continuous on the boundary of element K.
- $\boldsymbol{v}_h$ is a vector with second-order polynomial components on each edge of element K.
- $\Delta\boldsymbol{v}_h$ is constant in the interior of element K.

where Δ is the Laplace operator. By denoting the area of element K as $\left|\Omega^K\right|$, the corresponding degrees of freedom (DOFs) can be classified into the following three types [29]:

(i) The values of $\boldsymbol{v}_h$ at the n vertices of element K.

(ii) The values of $\boldsymbol{v}_h$ at the midpoints of n edges of element K.

(iii) The two moments of $\boldsymbol{v}_h$ with respect to the constant vectors $\boldsymbol{p}_1=\left[1,0\right]^T$ and $\boldsymbol{p}_2=\left[0,1\right]^T$ in element K, that is

$$\frac{1}{\left|\Omega^K\right|}\int_{\Omega^K}\boldsymbol{v}_h\cdot\boldsymbol{p}_1d\Omega^K;\ \frac{1}{\left|\Omega^K\right|}\int_{\Omega^K}\boldsymbol{v}_h\cdot\boldsymbol{p}_2d\Omega^K \tag{7}$$

Based on the DOFs of types (i)-(iii), the total number of DOFs of element K for the second-order VEM is $4n$+2 [30], and an arbitrary function $\boldsymbol{v}_h$ describing the displacement field of element K can be approximated by

$$\boldsymbol{v}_h=\sum_{i=1}^{4n+2}\mathrm{dof}_i\left(\boldsymbol{v}_h\right)\boldsymbol{\varphi}_i \tag{8}$$

where $\mathrm{dof}_i\left(\boldsymbol{v}_h\right)$ represents the ith DOF of $\boldsymbol{v}_h$ as given in types (i)-(iii) above, and $\boldsymbol{\varphi}_i$ is the ith vector-valued basis function (or shape function, see Appendix) of the local virtual element space $V_h\times V_h$ of element K with the following two properties [29]:

- **Property 1**: $\boldsymbol{\varphi}_i$ $(i=1,2,\cdots,4n+2)$ is a second-order polynomial on the element edge;

- **Property 2**: $\boldsymbol{\varphi}_i$ $(i=1,2,\cdots,4n+2)$ satisfies the Kronecker-delta property, that is, for the jth DOF of element K we have $\mathrm{dof}_j\left(\boldsymbol{\varphi}_i\right)=\delta_{ij}$, $i,j=1,2,\ldots,4n+2$.

In order to understand well the three types of DOFs defined in the second-order VEM, an illustrative example of a pentagon element K is given in Fig. 1. The five vertices and the edge midpoints are denoted as V1-V5 and M1-M5, respectively, and $\boldsymbol{v}_h\left(\bullet\right)$ denotes the value of $\boldsymbol{v}_h$ at the specified vertex or edge midpoint. Because $\boldsymbol{v}_h$ is a vector-valued function in which the two components represent the displacements in x- and y-directions, respectively, in the domain of element K, DOFs of types (i) and (ii) correspond directly to the displacements at the vertices and edge midpoints in both directions, respectively, and DOFs of type (iii) can be considered as the integral averages of displacements in both directions over the element domain Ω^K [22].

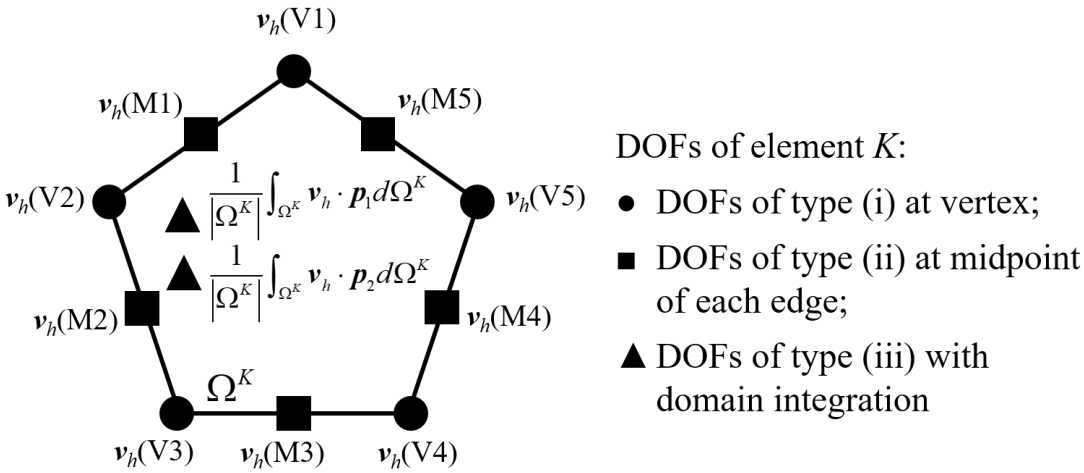

Fig. 1 DOFs of second-order VEM on pentagon element K

In a similar manner as the classical Galerkin FEM, the entry of the local element stiffness matrix $\boldsymbol{k}^K$ of element K is calculated using the above basis functions as

$$\left(\boldsymbol{k}^K\right)_{ij}=a^K\left(\boldsymbol{\varphi}_i,\boldsymbol{\varphi}_j\right)=\int_{\Omega^K}\boldsymbol{\sigma}\left(\boldsymbol{\varphi}_i\right):\boldsymbol{\varepsilon}\left(\boldsymbol{\varphi}_j\right)d\Omega^K \quad \text{for } i,j=1,2,\ldots,4n+2 \tag{9}$$

where the subscripts ij indicate the location of entry in $\boldsymbol{k}^K$. According to the basic formulation of second-order VEM, $\left(\boldsymbol{k}^K\right)_{ij}$ is obtained by introducing a projector $\prod^{\nabla}:V_h\times V_h\to P^2\times P^2$ which maps the function $\boldsymbol{v}_h$ in the space $V_h\times V_h$ onto the second-order polynomial space $P^2\times P^2$ satisfying the following orthogonality condition:

$$a^K\left(\boldsymbol{p}_\alpha,\prod^{\nabla}\boldsymbol{v}_h-\boldsymbol{v}_h\right)=0 \quad \text{for } \forall\boldsymbol{p}_\alpha\in P_2\times P_2 \text{ and } \boldsymbol{v}_h\in V_h\times V_h \tag{10}$$

where $\boldsymbol{p}_\alpha$, α=1,2,…,12 are the polynomial basis functions that span the second-order polynomial space $P_2 \times P_2$ (See Appendix). Then Eq. (9) is reformulated by using the projector Π^∇ as

$$\begin{aligned}&\left(\boldsymbol{k}^K\right)_{ij} = a^K\left(\Pi^\nabla \boldsymbol{\varphi}_i + \left(\boldsymbol{\varphi}_i - \Pi^\nabla \boldsymbol{\varphi}_i\right), \Pi^\nabla \boldsymbol{\varphi}_j + \left(\boldsymbol{\varphi}_j - \Pi^\nabla \boldsymbol{\varphi}_j\right)\right) = \\ &\underbrace{a^K\left(\Pi^\nabla \boldsymbol{\varphi}_i, \Pi^\nabla \boldsymbol{\varphi}_j\right)}_{\text{consistency}} + \underbrace{a^K\left(\boldsymbol{\varphi}_i - \Pi^\nabla \boldsymbol{\varphi}_i, \boldsymbol{\varphi}_j - \Pi^\nabla \boldsymbol{\varphi}_j\right)}_{\text{stability}} = \left(\boldsymbol{k}_c^K\right)_{ij} + \left(\boldsymbol{k}_s^K\right)_{ij} \quad \text{for } i, j = 1, 2, \ldots, 4n+2\end{aligned} \tag{11}$$

where $\Pi^\nabla \boldsymbol{\varphi}_i = \sum_{\alpha=1}^{12} S_{i,\alpha} \boldsymbol{p}_\alpha$, $\boldsymbol{p}_\alpha \in P^2 \times P^2$ is the image of basis function $\boldsymbol{\varphi}_i$ projected on the second-order polynomial space which is a linear combination of polynomial basis functions $\boldsymbol{p}_\alpha$ with coefficients $S_{i,\alpha}$, and $\left(\boldsymbol{k}^K\right)_{ij}$ can be thus considered as the sum of consistency term $\left(\boldsymbol{k}_c^K\right)_{ij}$ and stability term $\left(\boldsymbol{k}_s^K\right)_{ij}$ as shown in Eq. (11).

Thanks to the definition of projector Π^∇ and linearity of the strain tensor, the component-wise consistency term $\left(\boldsymbol{k}_c^K\right)_{ij}$ can be obtained explicitly as [30]

$$\begin{aligned}&\left(\boldsymbol{k}_c^K\right)_{ij} = \int_{\Omega^K} \boldsymbol{\sigma}\left(\Pi^\nabla \boldsymbol{\varphi}_i\right) : \boldsymbol{\varepsilon}\left(\Pi^\nabla \boldsymbol{\varphi}_j\right) d\Omega^K = \int_{\Omega^K} \boldsymbol{\sigma}\left(\sum_{\alpha=1}^{12} S_{i,\alpha} \boldsymbol{p}_\alpha\right) : \boldsymbol{\varepsilon}\left(\sum_{\beta=1}^{12} S_{j,\beta} \boldsymbol{p}_\beta\right) d\Omega^K \\ &= \sum_{\alpha=1}^{12}\sum_{\beta=1}^{12} S_{i,\alpha} S_{j,\beta} \int_{\Omega^K} \boldsymbol{\sigma}\left(\boldsymbol{p}_\alpha\right) : \boldsymbol{\varepsilon}\left(\boldsymbol{p}_\beta\right) d\Omega^K = \sum_{\alpha=1}^{12}\sum_{\beta=1}^{12} S_{i,\alpha} S_{j,\beta} a^K\left(\boldsymbol{p}_\alpha, \boldsymbol{p}_\beta\right) \\ &= \sum_{\alpha=1}^{12}\sum_{\beta=1}^{12} \boldsymbol{\Pi}_{i\alpha} \boldsymbol{\Pi}_{\beta j} \boldsymbol{G}_{\alpha\beta} = \left(\boldsymbol{\Pi}^T \boldsymbol{G} \boldsymbol{\Pi}\right)_{ij} \quad \text{for } i, j = 1, 2, \ldots, 4n+2\end{aligned} \tag{12}$$

where $\boldsymbol{\Pi}$ is the matrix representation of projector Π^∇, and matrix $\boldsymbol{G}$ is defined with entry $\boldsymbol{G}_{\alpha\beta} = a^K\left(\boldsymbol{p}_\alpha, \boldsymbol{p}_\beta\right)$, $\alpha, \beta = 1, 2, \cdots, 12$ (See Appendix A1 for detailed derivation).

As for calculation of stability term $\left(\boldsymbol{k}_s^K\right)_{ij}$, here we adopt the procedure provided by Gain et al. [20] which is derived with respect to the strain energy correction. First, define a (4n+2)×12 matrix $\boldsymbol{D}$ with entry as

$$\boldsymbol{D}_{i\alpha} = \text{dof}_i\left(\boldsymbol{p}_\alpha\right) \quad \text{for } i = 1, 2, \ldots, 4n+2 \text{ and } \alpha = 1, 2, \ldots, 12 \tag{13}$$

Next, by decomposing the image of projection $\Pi^\nabla \boldsymbol{\varphi}_i$ by the vector-valued functions in the local virtual element space $V_h \times V_h$, we can have the following matrix representation of another projection $\overline{\Pi}^\nabla : V_h \times V_h \to V_h \times V_h$ which maps the function in space $V_h \times V_h$ onto itself:

$$\bar{\boldsymbol{\Pi}}_{ij} = \mathrm{dof}_i\left(\prod^{\nabla}\varphi_j\right) = \mathrm{dof}_i\left(\sum_{\beta=1}^{12} S_{j,\beta}\boldsymbol{p}_\beta\right) = \sum_{\beta=1}^{12}\boldsymbol{D}_{i\beta}\boldsymbol{\Pi}_{\beta j} = \left(\boldsymbol{D}\boldsymbol{\Pi}\right)_{ij} \quad \text{for } i,j = 1,2,\cdots,4n+2 \tag{14}$$

where $\bar{\boldsymbol{\Pi}}$ is the matrix representation of projection $\bar{\prod}^{\nabla}$, and the detailed calculations of $\boldsymbol{D}$ and $\bar{\boldsymbol{\Pi}}$ are given in Appendix A2. Based on Eq. (14), the stability term $\left(\boldsymbol{k}_s^K\right)_{ij}$ is calculated as

$$\left(\boldsymbol{k}_s^K\right)_{ij} = \gamma\tau^*\left(\boldsymbol{I}-\bar{\boldsymbol{\Pi}}\right)_i^T\left(\boldsymbol{I}-\bar{\boldsymbol{\Pi}}\right)_j \quad \text{for } i,j = 1,2,\ldots,4n+2 \tag{15}$$

where $\boldsymbol{I}$ is the $(4n+2)\times(4n+2)$ identity matrix; γ is the user-defined parameter which can be chosen as 1 for elastic problem, and τ^* is calculated as [20]

$$\tau^* = \frac{\left|\Omega^K\right|\mathrm{trace}\left(\mathbb{C}\right)}{\mathrm{trace}\left(\begin{pmatrix}\boldsymbol{D}_4 & \boldsymbol{D}_5 & \cdots & \boldsymbol{D}_{12}\end{pmatrix}^T\begin{pmatrix}\boldsymbol{D}_4 & \boldsymbol{D}_5 & \cdots & \boldsymbol{D}_{12}\end{pmatrix}\right)} \tag{16}$$

where $\mathrm{trace}(\cdot)$ denotes the sum of the diagonal components and $\left(\boldsymbol{D}_4,\boldsymbol{D}_5,\cdots,\boldsymbol{D}_{12}\right)$ is a part of the matrix $\boldsymbol{D}$ from column 4 to 12. Hence, through Eqs. (12) to (16), one can calculate all the entries in local stiffness matrix $\boldsymbol{k}^K$ of element K, and the global stiffness matrix can be obtained by assembling all the local stiffness matrices in the same manner as the classical Galerkin FEM.

In addition, based on Eqs. (6) and (8), the local VEM loading term for element K corresponding to the traction vectors acting on the boundary takes the form

$$\begin{aligned} f^K\left(\boldsymbol{v}_h\right) &= \int_{\partial\boldsymbol{\Omega}_t^K}\boldsymbol{v}_h\cdot\boldsymbol{t}d\partial\boldsymbol{\Omega}_t^K = \int_{\partial\boldsymbol{\Omega}_t^K}\left(\sum_{i=1}^{4n+2}\mathrm{dof}_i\left(\boldsymbol{v}_h\right)\boldsymbol{\varphi}_i\right)\cdot\boldsymbol{t}d\partial\boldsymbol{\Omega}_t^K \\ &= \sum_{i=1}^{4n+2}\mathrm{dof}_i\left(\boldsymbol{v}_h\right)\int_{\partial\boldsymbol{\Omega}_t^K}\boldsymbol{\varphi}_i\cdot\boldsymbol{t}d\partial\boldsymbol{\Omega}_t^K \end{aligned} \tag{17}$$

and the entry of element loading vector is $\int_{\partial\boldsymbol{\Omega}_t^K}\boldsymbol{\varphi}_i\cdot\boldsymbol{t}d\partial\boldsymbol{\Omega}_t^K$, for $i=1,2,\cdots,4n+2$. Note that Eq. (17) is computable using numerical integration because $\boldsymbol{\varphi}_i$ is a second-order polynomial on the element edge and satisfying the Kronecker-delta property as given above. Therefore, the computation procedure of Eq. (17) follows the classical Galerkin FEM [30]. Moreover, because the concentrated loads at nodes can be directly put into the element loading vector at the associated DOF at which the load is applied, it is omitted in Eq. (17) for simplicity.

3. Contact formulation using VEM

In this section, the formulation of node-to-node contact analysis for non-matching meshes is presented using second-order VEM with normal and frictional contact with stick condition. Deformation of the structure in contact is assumed to be small.

3.1 Node-to-Node contact kinematics

Suppose two elastic bodies B^1 and B^2 come into contact with matching meshes along the contact interface as shown in Fig. 2, where one node pair i is taken as an example for illustrating the procedure. Denote the displacements of nodes P_i^1 and P_i^2 of node pair i as $\boldsymbol{u}_i^1$ and $\boldsymbol{u}_i^2$, respectively, and the outward normal vector at node P_i^1 as $\mathbf{n}_i^1$. The gap between nodes P_i^1 and P_i^2 reads

$$g_{Ni} = \left(\boldsymbol{u}_i^2 - \boldsymbol{u}_i^1\right) \cdot \boldsymbol{n}_i^1 + g_i \tag{18}$$

where g_i is the initial gap between nodes P_i^1 and P_i^2.

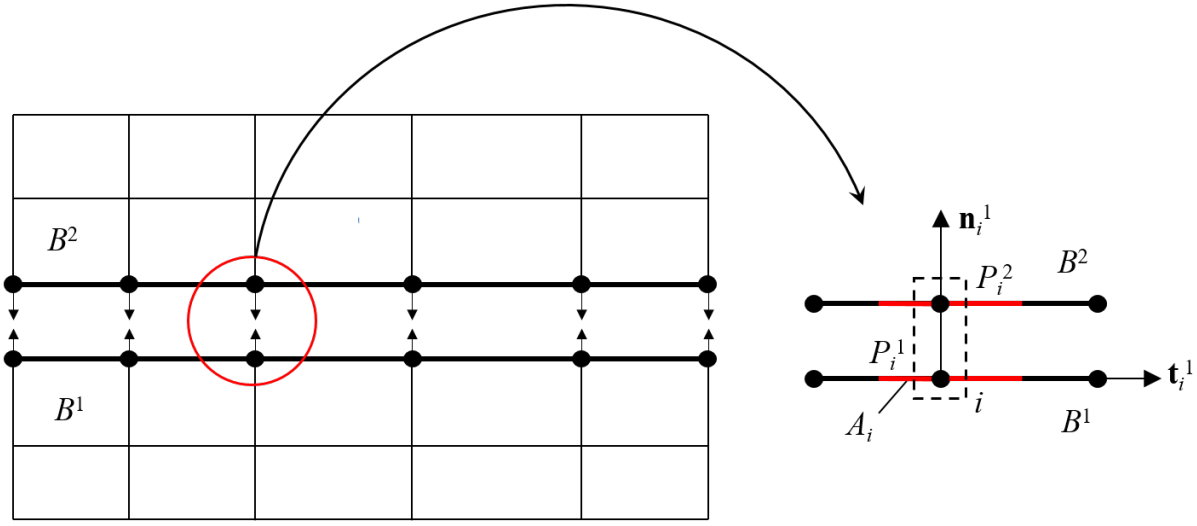

Fig. 2 Contact interface with matching meshes

Based on the Lagrange multiplier method and the non-penetrating condition for normal contact, the variation of normal contact energy of node i to be added to the total potential energy corresponding to the deformation of B^1 and B^2 is written as [2]

$$\lambda_{Ni}\delta g_{Ni} = \lambda_{Ni}\left(\delta\boldsymbol{u}_i^2 - \delta\boldsymbol{u}_i^1\right) \cdot \mathbf{n}_i^1 A_i \tag{19}$$

and the variation of enforced non-penetrating condition for normal contact is written as

$$\delta\lambda_{Ni} g_{Ni} = \delta\lambda_{Ni}\left(\left(\boldsymbol{u}_i^2 - \boldsymbol{u}_i^1\right) \cdot \mathbf{n}_i^1 + g_i\right) A_i \tag{20}$$

where λ_{Ni} is the Lagrange multiplier for non-penetrating condition of node pair i; A_i is the contact area associated with node pair i as shown in Fig. 2. Note that the contact area is assumed to be a half of the sum of areas of the two adjacent contact segments. Combing Eqs. (19) and (20) with the variations of potential energies of B^1 and B^2, the matrix form of variation of total potential energy of the system related to a single contact node pair i can be given as [2]

$$\begin{bmatrix} \boldsymbol{K}^2 & & \boldsymbol{C}^2 \\ & \boldsymbol{K}^1 & \boldsymbol{C}^1 \\ \left(\boldsymbol{C}^2\right)^T & \left(\boldsymbol{C}^1\right)^T & 0 \end{bmatrix} \begin{bmatrix} \boldsymbol{u}^2 \\ \boldsymbol{u}^1 \\ \lambda_{Ni} \end{bmatrix} = \begin{bmatrix} \boldsymbol{f}^2 \\ \boldsymbol{f}^1 \\ g_i \end{bmatrix} \tag{21}$$

where $\boldsymbol{K}^1$ and $\boldsymbol{K}^2$ are the global stiffness matrices of elastic bodies B^1 and B^2, respectively; $\boldsymbol{f}^1$ and $\boldsymbol{f}^2$ are the external loads applied respectively at the elastic bodies B^1 and B^2, and $\boldsymbol{u}^1$ and $\boldsymbol{u}^2$ are the corresponding displacement vectors to be obtained; $\boldsymbol{C}^1$ and $\boldsymbol{C}^2$ are two vectors filled with zeros except for the two components corresponds to the two DOFs of nodes P_i^1 and P_i^2, respectively, i.e., $\boldsymbol{C}^1$ and $\boldsymbol{C}^2$ can be written as follows [2]:

$$\begin{aligned} \boldsymbol{C}^1 &= \left[0, \cdots, -n_{i,x}^1, \cdots, -n_{i,y}^1, \cdots, 0\right] \\ \boldsymbol{C}^2 &= \left[0, \cdots, n_{i,x}^1, \cdots, n_{i,y}^1, \cdots, 0\right] \end{aligned} \tag{22}$$

where $n_{i,x}^1$ and $n_{i,y}^1$ are the components in the outward normal vector $\mathbf{n}_i^1 = \left[n_{i,x}^1, n_{i,y}^1\right]$.

Moreover, the variation of frictional contact of node pair i with stick condition contributing to the total potential energy of the system is formulated using penalty method as [2]

$$\varepsilon_T g_{Ti} \cdot \delta g_{Ti} A_i = \varepsilon_T \left[\left(\left(\boldsymbol{u}_i^2 - \boldsymbol{u}_i^1\right)^T \mathbf{t}_i^1 \right) \left(\left(\delta \boldsymbol{u}_i^2 - \delta \boldsymbol{u}_i^1\right)^T \mathbf{t}_i^1 \right) \right] A_i \tag{23}$$

where $g_{Ti} = \left(\boldsymbol{u}_i^2 - \boldsymbol{u}_i^1\right)^T \mathbf{t}_i^1$ is the relative displacement of node pair i in tangential direction and $\mathbf{t}_i^1$ is the normalized tangential vector as shown in Fig. 2. By introducing the vector $\mathbf{T}_i^1 = \left[\mathbf{t}_i^{1T} \quad -\mathbf{t}_i^{1T}\right]^T$, Eq. (23) can be reformulated in a matrix form as

$$\varepsilon_T g_{Ti} \cdot \delta g_{Ti} A_i = \varepsilon_T \left[\delta \boldsymbol{u}_i^2 \quad \delta \boldsymbol{u}_i^1\right] \mathbf{T}_i^1 \left(\mathbf{T}_i^1\right)^T \begin{bmatrix} \boldsymbol{u}_i^2 \\ \boldsymbol{u}_i^1 \end{bmatrix} A_i = \left[\delta \boldsymbol{u}_i^2 \quad \delta \boldsymbol{u}_i^1\right] \boldsymbol{K}_{Ti} \begin{bmatrix} \boldsymbol{u}_i^2 \\ \boldsymbol{u}_i^1 \end{bmatrix} \tag{24}$$

where $\boldsymbol{K}_{Ti} = \varepsilon_T \mathbf{T}_i^1 \left(\mathbf{T}_i^1\right)^T A_i$ is the 4×4 local tangent stiffness matrix. By extending $\boldsymbol{K}_{Ti}$ to the global tangent stiffness matrix $\boldsymbol{K}_T$ in which the components associated with the DOFs of P_i^1 and P_i^2 are the components of $\boldsymbol{K}_{Ti}$ and the others are 0, Eq. (21) is further modified to consider the frictional contact with stick condition as follows:

$$\begin{bmatrix} \overline{\boldsymbol{K}} + \boldsymbol{K}_T & \overline{\boldsymbol{C}} \\ \overline{\boldsymbol{C}}^T & 0 \end{bmatrix} \begin{bmatrix} \overline{\boldsymbol{u}} \\ \lambda_{Ni} \end{bmatrix} = \begin{bmatrix} \overline{\boldsymbol{f}} \\ g_i \end{bmatrix} \tag{25}$$

where $\overline{\boldsymbol{K}} = \begin{bmatrix} \boldsymbol{K}^2 & \\ & \boldsymbol{K}^1 \end{bmatrix}$, $\overline{\boldsymbol{C}} = \left[\boldsymbol{C}^2 \quad \boldsymbol{C}^1\right]^T$, $\overline{\boldsymbol{u}} = \left[\boldsymbol{u}^{2T} \quad \boldsymbol{u}^{1T}\right]^T$ and $\overline{\boldsymbol{f}} = \left[\boldsymbol{f}^{2T} \quad \boldsymbol{f}^{1T}\right]^T$.

3.2 Node insertion with non-matching meshes

The VEM discretization scheme allows hanging nodes in the mesh and thus makes it possible to arbitrarily insert new nodes to the existing elements [17]. In this way, the node-to-node contact pair can be easily constructed for non-matching meshes at the contact interface, and the contact analysis can be proceeded at the node level as discussed above.

Since in VEM the integral operations for computing the entries in Eqs. (12) and (15) are all implemented on the element boundary (see Appendix for more details), inserting a new node to an element only adds one more loop for extending the element stiffness matrix with the additional DOFs of the new node. Therefore, the cost increased by inserting a new node to transform non-matching meshes into matching meshes at the contact interface is minimal [17].

To clearly illustrate the general node insertion procedure using VEM, the contact model illustrated in Sec. 3.2 is modified so that points P_i^1 and P_i^2 do not coincide at the contact interface, forming simple non-matching meshes as shown in Fig. 3(a). The elements e^1 and e^2 before inserting a new node are both quadrilaterals with four edges. However, when P_i^1 and P_i^2 are inserted to elements e^2 and e^1, respectively, as shown in Fig. 3(b), they both become pentagons with one hanging node, making the two consecutive edges at the contact boundary to form a straight line. However, the rest of the elements in B^1 and B^2 remains unchanged. Therefore, by using VEM, the adaption of non-matching meshes to matching meshes is very simple, and Eq. (25) can be used for contact analysis.

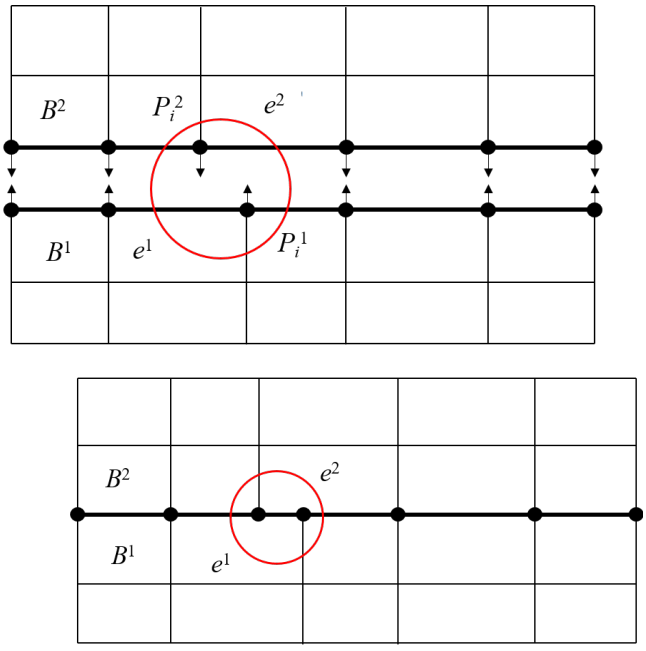

(a) (b)

Fig. 3 Adaption process of non-matching contact nodes; (a) Initial non-matching meshes; (b) Matching meshes after inserting new nodes

4. Numerical examples

In this section four numerical examples including the patch test are investigated to demonstrate the effectiveness of the proposed method for 2-dimensional contact analysis of plates consisting of irregular elements. Plane stress condition is considered for all examples, and the contact analysis is implemented using MATLAB [31]. The contact pairs are determined as follows: firstly select the possible node pairs at the initial contact interface and assume they will be in contact after deformation, and then repeat the contact analysis until all the normal contact forces (i.e., the values of Lagrangian multipliers in Eq. 25) are positive. After that if there are still penetrations among the elastic bodies, select the corresponding node pairs and assume they will also be in contact after deformation, and again repeat the contact analysis until all the normal contact forces are positive.

4.1 Example 1

The first example is a patch test with irregular elements using the second-order VEM to check the correct transfer of contact pressure [17, 32]. The model of two 6×2 (mm) blocks is shown in Fig. 4 (a) in which contact interface is marked by red line. For both blocks, Young's modulus is 7000 MPa and Poisson's ratio is 0.3. A uniform downward distributed load of 100 N/mm is applied at the top surface of upper block, and the support conditions are given in Fig. 4 (a) for both blocks to model axial compression.

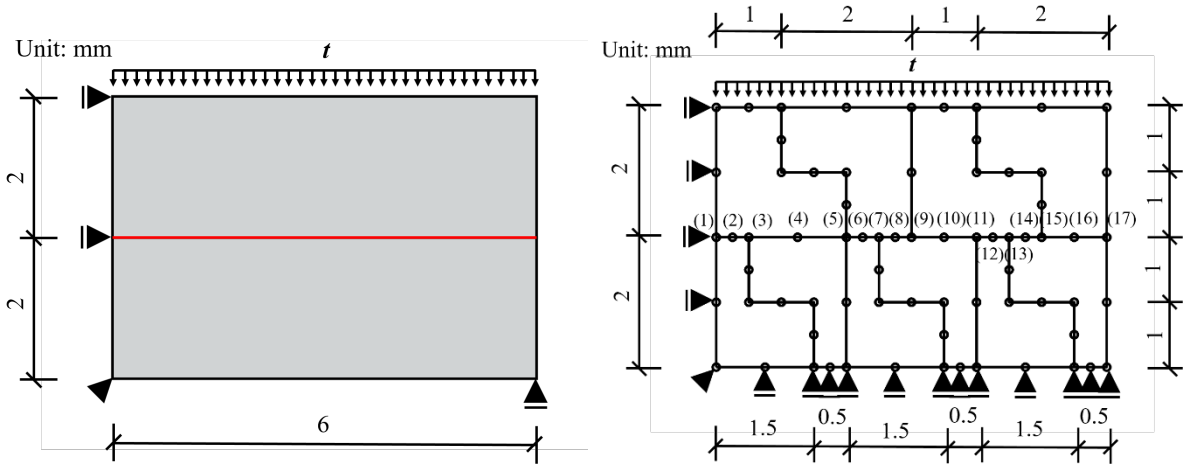

(a) (b)

Fig. 4 Model of Example 1; (a) Geometry models of two elastic blocks, (b) Second-order VEM discretization

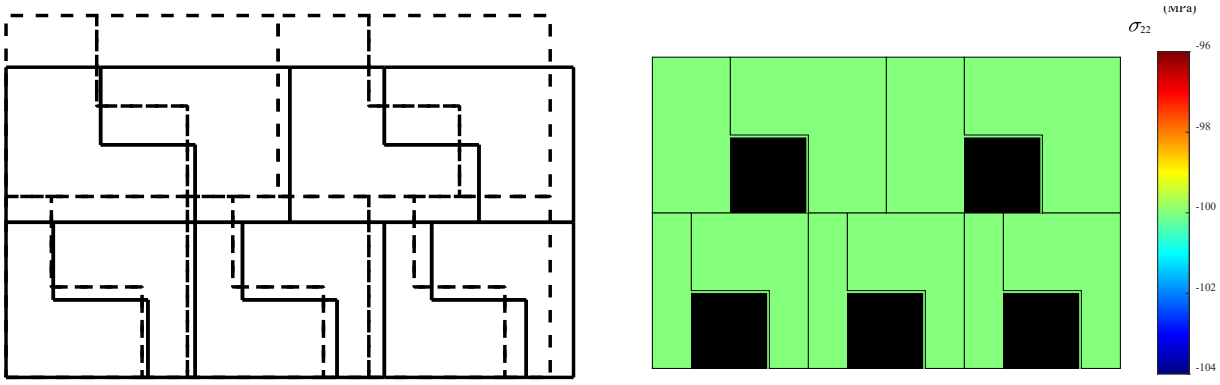

(a) (b)

Fig. 5 Results of Example 1; (a) Deformed shape, (b) Stress contour of σ_{22}

The two blocks are discretized with different non-convex meshes as shown in Fig. 4(b) in which the lower and upper blocks have six and four L-shape elements, respectively, leading to an initial non-matching contact interface. By using the node insertion algorithm as described in Sec. 3.2, the nodes located at the element edge of the other block are inserted to each other and therefore there are 17 node-to-node contact pairs in total along the contact interface. The results of deformed shape and stress are shown in Figs. 5(a) and (b), respectively, where the deformation is scaled by the factor 10 for clear observation of deformation. As we can see from Fig. 5, the second-order VEM passes the patch test where a constant vertical stress contour of $\sigma_{22} = 100$ MPa and deformation of axial compression are obtained, whereas the classical node-to-segment or segment-to-segment discretization may not be able to transfer the contact pressure accurately if the meshes are non-matching at the contact interface [11, 17]. Moreover, as pointed out by Papadopoulos and Taylor [10] and Xing et al. [14], the deviation of stress and displacement of classical node-to-segment or segment-to-segment discretization depends on the non-uniformness of the meshes at the contact interface, and the use of second-order element will produce a larger deviation compared to linear element.

4.2 Example 2

The second example is a contact problem of two hollow cylinders subjected to internal uniform pressure is studied. Due to the symmetry, only a quarter of the model is calculated as shown in Fig. 6(a) and the contact interface is marked by red line. According to Ref. [14], the radii of the hollow cylinders are $R_i = 0.9$ m, $R_m = 1.0$ m and $R_o = 1.1$ m. Young's modulus is $E = 100$ MPa and the Poisson's ratio is $\nu = 0.3$ for both hollow cylinders. The boundary conditions are $u_x = 0$ at $x = 0$, $u_y = 0$ at $y = 0$ and $p = 10$ kN/m at the inner cylinder. The exact analytical solutions of the radial displacement u_r, radial stress σ_{rr} and circumferential stress $\sigma_{\theta\theta}$ at radius $r = \sqrt{x^2 + y^2}\ (R_i \le r \le R_o)$ are given as follows [14]:

$$u_r(r)=\frac{1}{E}\frac{pR_i^2}{R_o^2-R_i^2}\left((1-v)r+\frac{R_o^2(1+v)}{r}\right) \tag{26}$$

$$\sigma_{rr}(r)=\frac{pR_i^2}{R_o^2-R_i^2}\left(1-\frac{R_o^2}{r^2}\right) \tag{27}$$

$$\sigma_{\theta\theta}(r)=\frac{pR_i^2}{R_o^2-R_i^2}\left(1+\frac{R_o^2}{r^2}\right) \tag{28}$$

Firstly, the effects of small edges on the accuracy and robustness of the proposed method are investigated. The two cylinders are discretized by quadrilateral element with the mesh ratio 3:4 between the numbers of elements of inner and outer hollow cylinders, resulting in a non-matching contact interface as shown by the red line in Fig. 7(a). Based on Ref. [33], a very small edge of length $l=1\times10^{-4}$m is generated on the contact interface at the angle of $\theta=\pi/5$with counterclockwise direction shown in Fig. 7(a), which is about 0.1% of the element edge [33]. For comparison purpose, a discretization model without the small edge is also studied as shown in Fig. 7(b), which has the same mesh ratio 3:4. Then, the accuracy is investigated by comparing the displacement result $u_{r,\mathrm{vem}}$ and the stress results $\sigma_{rr,\mathrm{vem}}$ and $\sigma_{\theta\theta,\mathrm{vem}}$ obtained by the proposed method, respectively, to the analytical solutions obtained by Eqs. (26)-(28), and the errors in displacement and stress results are measured by the following equations [14][25]:

$$e_u=\frac{\sqrt{\sum_{K\in\Omega}\left(u_{r,\mathrm{vem}}|_K-u_r|_K\right)^2}}{\sqrt{\sum_{K\in\Omega}\left(u_r|_K\right)^2}};\ e_{\sigma_{rr}}=\frac{\sqrt{\sum_{K\in\Omega}\left(\sigma_{rr,\mathrm{vem}}|_K-\sigma_{rr}|_K\right)^2}}{\sqrt{\sum_{K\in\Omega}\left(\sigma_{rr}|_K\right)^2}};\ e_{\sigma_{\theta\theta}}=\frac{\sqrt{\sum_{K\in\Omega}\left(\sigma_{\theta\theta,\mathrm{vem}}|_K-\sigma_{\theta\theta}|_K\right)^2}}{\sqrt{\sum_{K\in\Omega}\left(\sigma_{\theta\theta}|_K\right)^2}}; \tag{29}$$

where the subscript K denotes the result of element K. For simplicity, only the displacement and stress values at the vertices and the midpoints of edges of each element are used in Eq. (29).

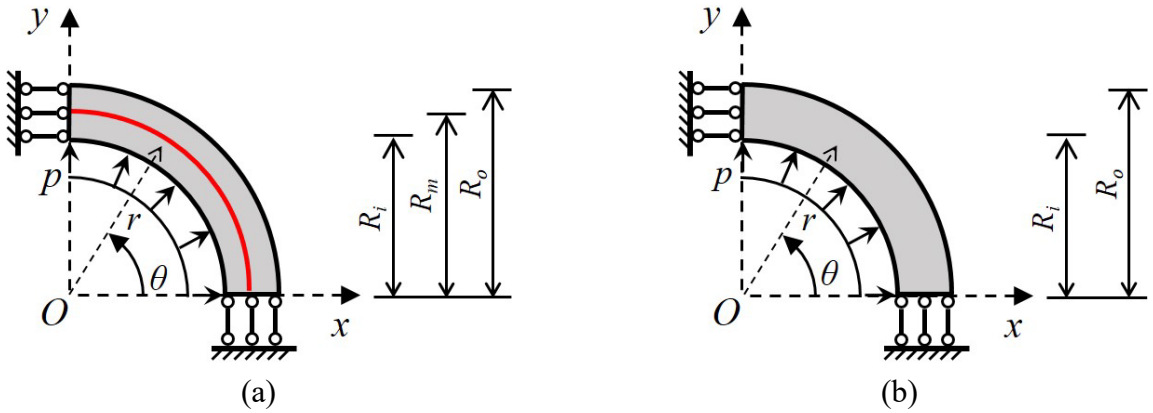

Fig. 6 Model of hollow cylinder under internal pressure: (a) Contact problem; (b) One-piece hollow cylinder

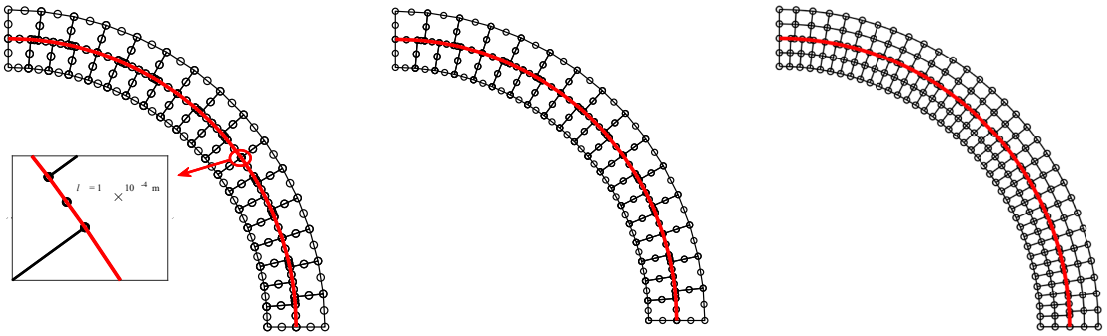

(a) (b) (c)

Fig. 7 Meshes of two contact hollow cylinders (a) Second-order VEM with small edge; (b) Second-order VEM without small edge; (c) Linear VEM

The errors and number of DOFs are listed in Table 1, and the displacement and stress results of $u_{r,\mathrm{vem}}$, $\sigma_{rr,\mathrm{vem}}$ and $\sigma_{\theta\theta,\mathrm{vem}}$ with and without small edge, as well as the analytical solutions u_r, σ_{rr} and $\sigma_{\theta\theta}$, are displayed in Figs. 8-10, respectively. It can be observed from Figs. 8-10 that compared to the analytical solutions, both the results with and without small edge have the similar value and distribution among the two hollow cylinders, and the corresponding errors are also close to each other, while the error with small edge is slightly larger than those without small edge. The details of displacements of nodes on the contact surface are displayed in Fig. 11 for further discussion. It can be seen that when the small edge exists at $\theta = \pi/5$, the nodal displacements become slightly oscillatory between $\theta = 3\pi/16$ and $\theta = 5\pi/16$, where the three nodal displacements of the small edge look like a vertical line at $\theta = \pi/5$ in Fig. 11. However, the general variation of the nodal displacements with small edge around the analytical solution is still close to those without small edge, indicating the proposed second-order VEM is accurate enough in small deformation contact problem with small edge on the contact interface. This property is also investigated and addressed in the linear elasticity problem with theoretical justification [33][34], where the accuracy and convergence rate are not noticeably deteriorated by the presence of small edges in 2D and small faces in 3D.

Table 1 Comparison result of second-order and linear VEM

Method	Number of DOFs	Error e_u	Error $e_{\sigma_{rr}}$	Error $e_{\sigma_{\theta\theta}}$
Second-order VEM with small edge	540	0.0121	0.0509	0.0121
Second-order VEM without small edge	532	0.0118	0.0496	0.0116
Linear VEM without small edge	532	0.0146	0.2448	0.0304

Moreover, the computational efficiency of the proposed method is also investigated by comparing the results obtained by the proposed method and linear VEM, and the corresponding linear VEM discretization is displayed in Fig. 7(c), which has the same mesh ratio 3:4 and

number of DOFs as Fig. 7(b). The errors and displacement and stress results obtained by linear VEM are listed in Table 1 and Fig. 12, respectively. It can be observed from Figs. 9, 10 and 12 that because the results in Fig. 9 are similar to the analytical solutions in Fig. 10, respectively, the second-order VEM is able to capture the nonlinear radial displacement field using second-order polynomial; On the other hand, the linear VEM can only approximate the nonlinear radial displacement field by the piece-wise linear polynomial, leading to a more oscillatory displacement field on the contact interface than that obtained by second-order VEM, and the checkboard phenomenon appears in both radial and circumferential stress fields due to the discontinuity of stress among elements. Therefore, although both linear and second-order VEM have the same number of DOFs, the second-order VEM is able to achieve higher accuracy than linear VEM with a coarse mesh on the model, which is very helpful for engineers and researchers to handle contact problems with complex geometry.

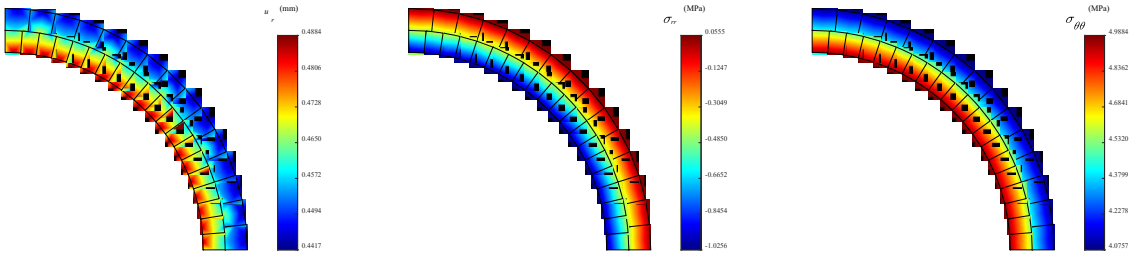

(a) (b) (c)

Fig. 8 Results obtained by second-order VEM with small edge (a) $u_{r,\mathrm{vem}}$; (b) $\sigma_{rr,\mathrm{vem}}$; (c) $\sigma_{\theta\theta,\mathrm{vem}}$

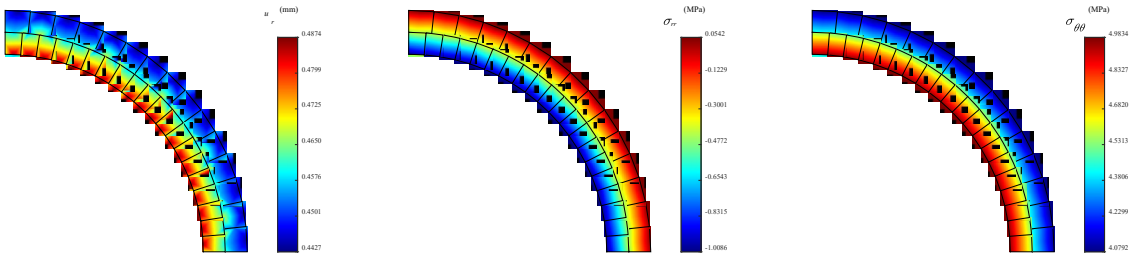

(a) (b) (c)

Fig. 9 Results obtained by second-order VEM without small edge (a) $u_{r,\mathrm{vem}}$; (b) $\sigma_{rr,\mathrm{vem}}$; (c) $\sigma_{\theta\theta,\mathrm{vem}}$

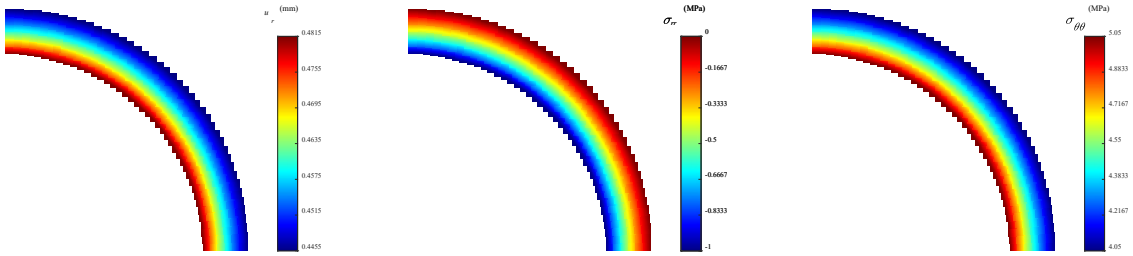

(a) (b) (c)

Fig. 10 Analytical solution of displacement and stress (a) u_r ; (b) σ_{rr} ; (c) $\sigma_{\theta\theta}$

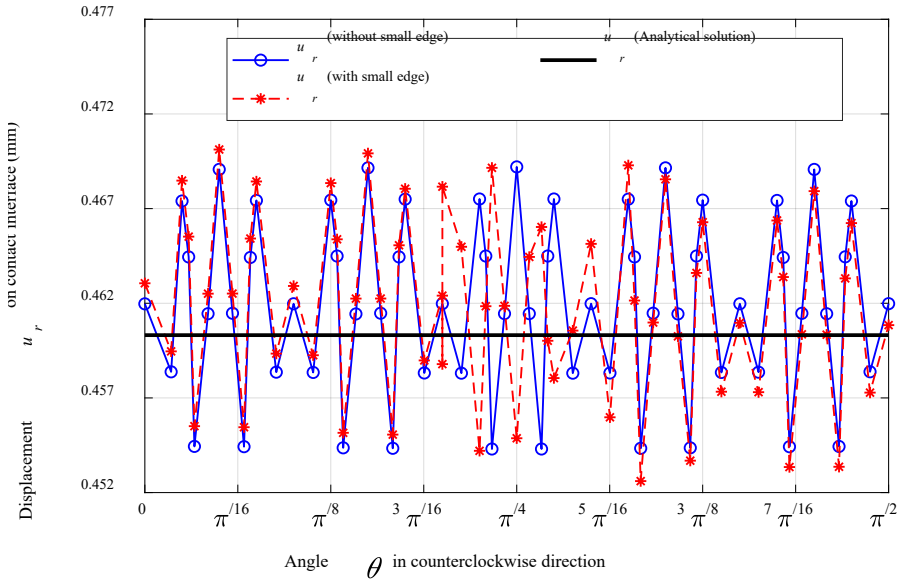

Fig. 11 Displacement results obtained by second-order VEM on the contact interface

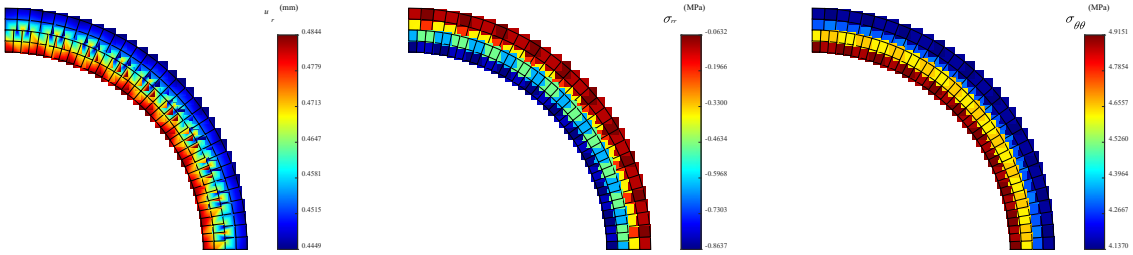

(a) (b) (c)

Fig. 12 Results obtained by linear VEM without small edge (a) $u_{r,\mathrm{vem}}$; (b) $\sigma_{rr,\mathrm{vem}}$; (c) $\sigma_{\theta\theta,\mathrm{vem}}$

Besides, the mesh refinement for the convergence study of the proposed method is implemented by decreasing the element size as shown in Fig. 13, where the contact interface is denoted by the red line. The convergence study in terms of linear elasticity problem is also investigated by merging the two hollow cylinders into one-piece hollow cylinder as shown in Fig. 6(b), and the corresponding mesh refinement is left here for simplicity. The convergence results of displacement and stress errors versus average element size are displayed in Fig. 14, and it can be observed that for both contact and linear elasticity problems the convergence rate of the displacement error is with the optimal order 2 as expected [22][35], and the convergence rates of both stress errors are around 1, indicating that both contact and linear elasticity modelings will converge to the exact solution.

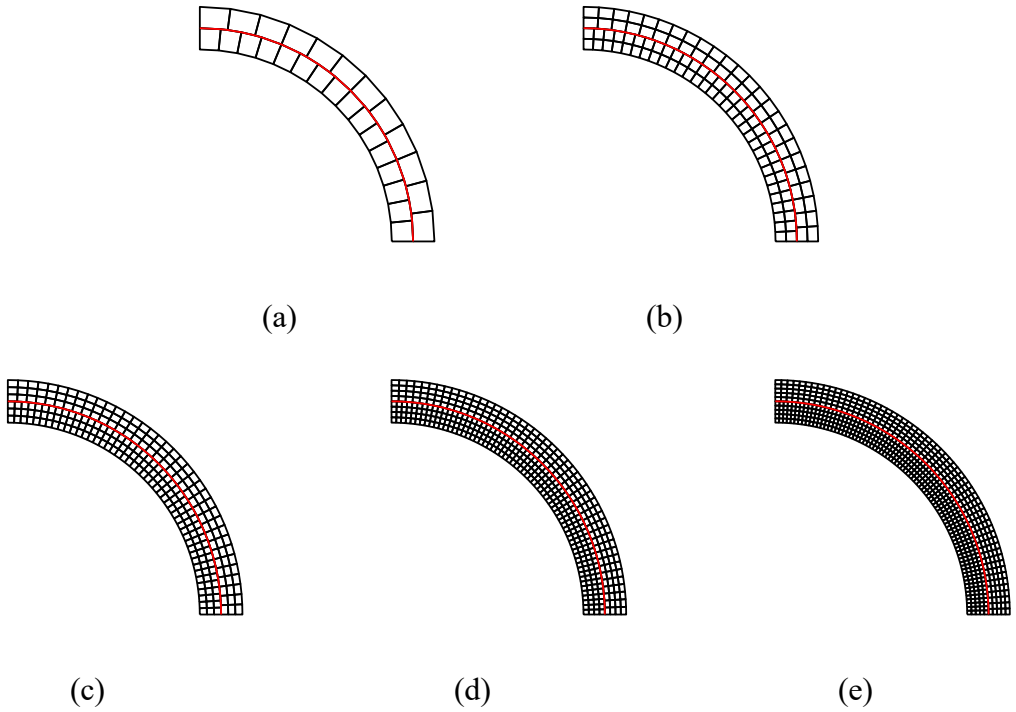

Fig. 13 Mesh refinement of two contact hollow cylinders with different average element size (a) $h^K = 0.1508$; (b) $h^K = 0.0755$; (c) $h^K = 0.0503$; (d) $h^K = 0.0377$; (e) $h^K = 0.0302$;

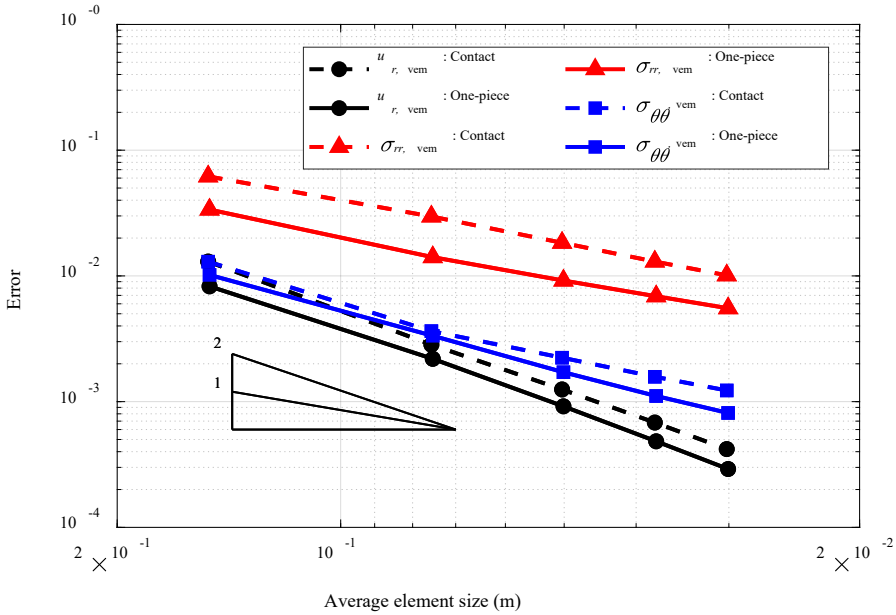

Fig. 14 Error versus average element size

4.3 Example 3

The third example is a multi-body contact problem of a rectangular frame infilled with four blocks as shown in Fig. 15(a). The structure is fixed at the bottom left and right, and a horizontal load $F = 1000$ N is applied at the top left. The corresponding second-order VEM discretization is given in Fig. 15(b), where the rectangular frame is divided into 22 elements, and each block is simulated by only one element. Young's modulus and Poisson's ratio for the rectangular frame and the blocks are 3×10^4 MPa and 0.3, respectively. In addition, for comparison purpose the rectangular frame without the four infilled blocks is also investigated with the same loading and supporting conditions as well as the material parameters.

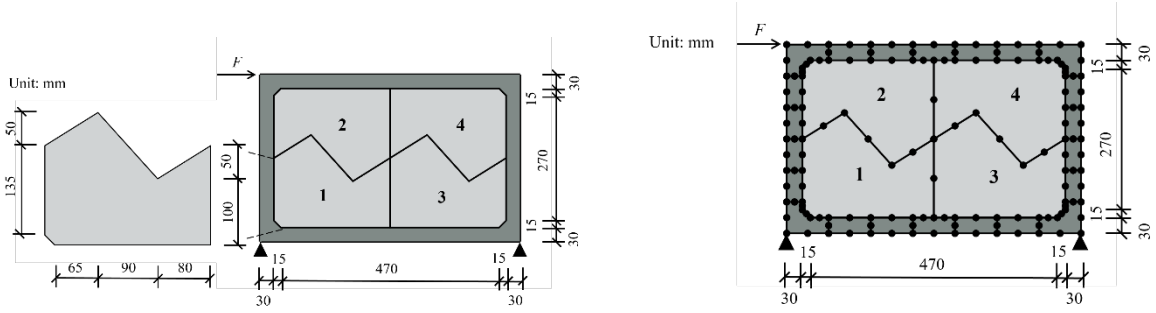

(a) (b)

Fig. 15 Model of Example 3; (a) Geometry models of rectangle frame and four infilled blocks, (b) Second-order VEM discretization

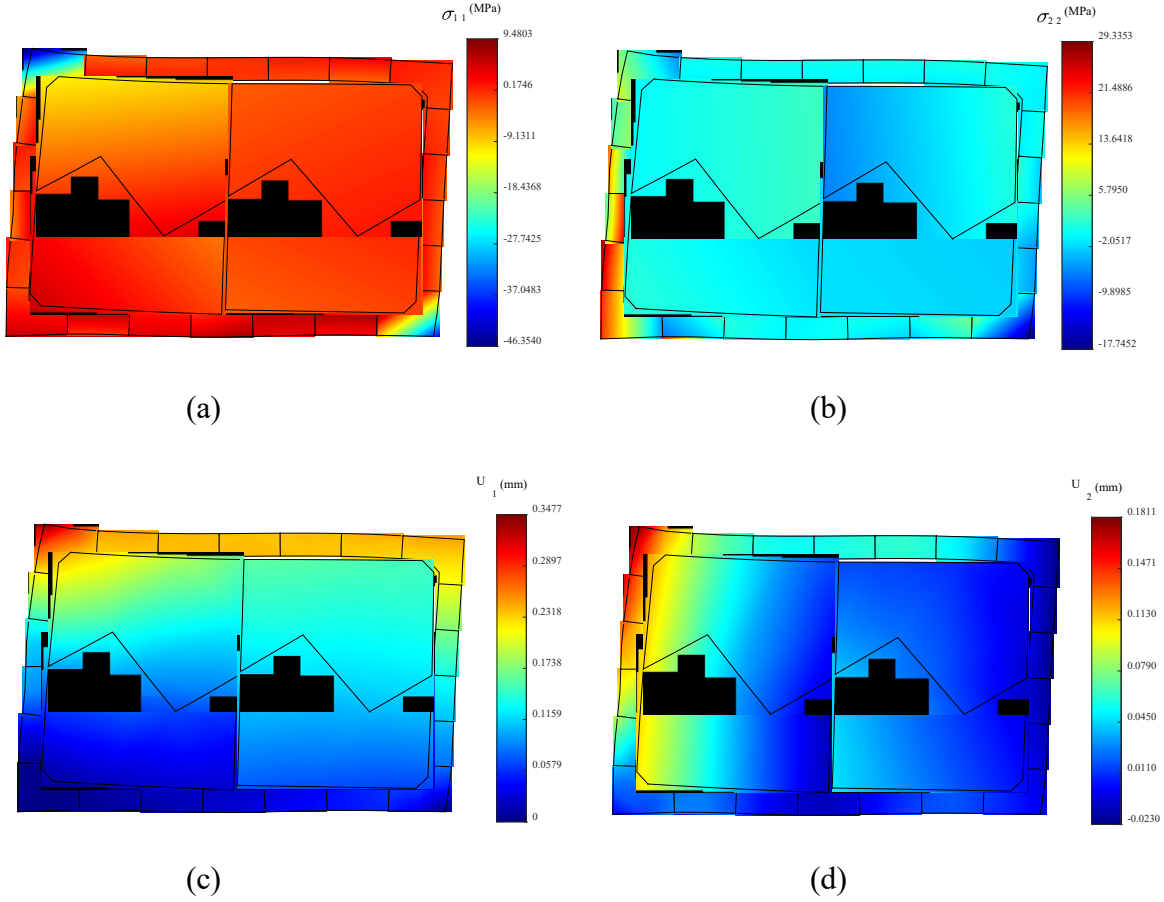

Fig. 16 Results of Example 3; (a) Stress contour of σ_{11}, (b) Stress contour of σ_{22}, (c) Displacement contour of U_1, (d) Displacement contour of U_2

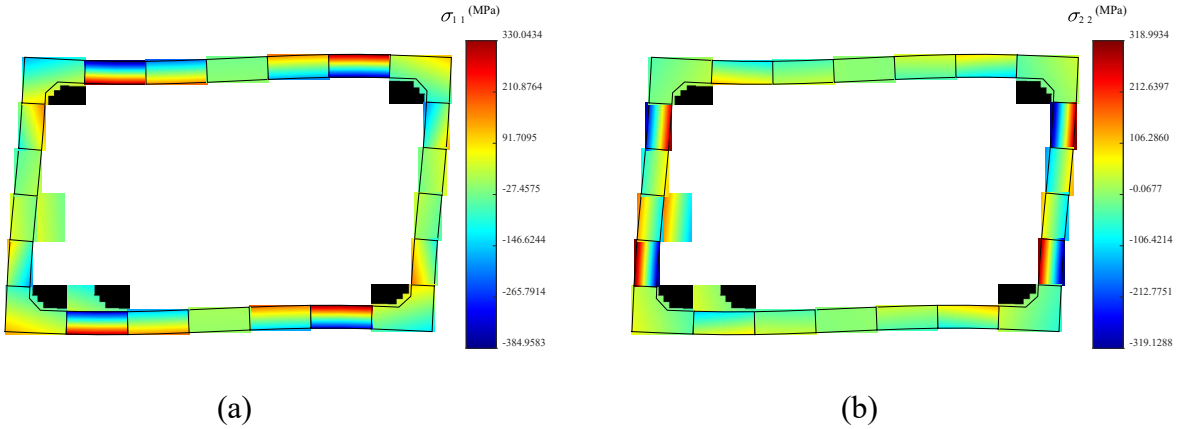

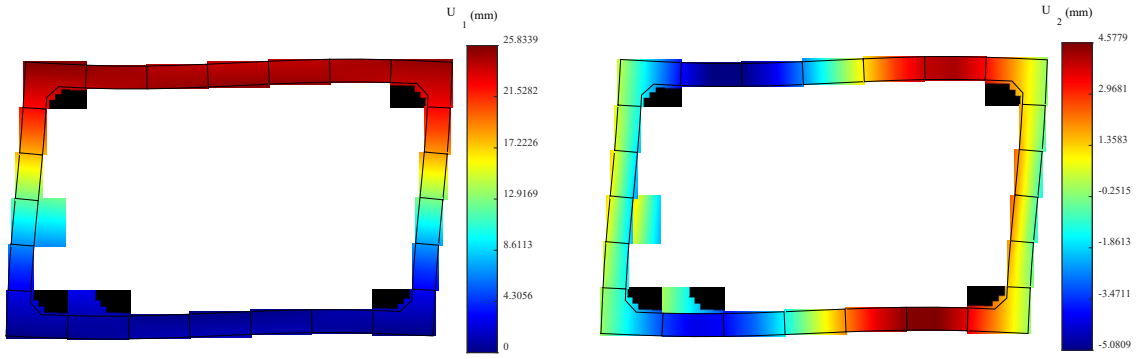

(c) (d)

Fig. 17 Results of Example 3 without infilled blocks, (a) Stress contour of σ_{11}, (b) Stress contour of σ_{22}, (c) Displacement contour of U_1, (d) Displacement contour of U_2

The contours of stress and displacement of the structures with and without infilled blocks are displayed in Figs. 16 and 17, respectively, with deformed shapes in which the deformations of frame and blocks are scaled by the factor 100. Note that U_1 and U_2 denote the horizontal and vertical displacement components, respectively. Comparing Figs. 16 and 17, it is obvious that the stress level and displacement of the structure are significantly reduced when the blocks are infilled in the frame, indicating that the infilled blocks have a great influence on increasing the stiffness against the horizontal external load. The main reason for this is that without infilled blocks the structure resists the horizontal load mainly by bending deformations, while with infilled blocks the rectangular frame and blocks can work together against the horizontal load. Specifically, σ_{11} in Fig. 16(a) is under compression at the top left and bottom right of the frame, meaning that the horizontal force is transmitted from the loading point in a diagonal direction to the support at the bottom right by the contact between frame and blocks and among blocks. By contrast, in Fig. 16(a), the beam has very high level of bending stress in the elements connected to the beam-column joints, and similar phenomenon of high bending stress can also be observed in Fig. 17(b). Since the infilled blocks increase the stiffness of the whole structure, deformations of the frame are restricted by the infilled blocks as shown in Figs. 16(c) and (d), and the largest displacement primarily exists around the loading point. On the other hand, the horizontal displacement U_1 of the structure without infilled blocks has large value along the top beam due to the small bending stiffness of beams and columns as shown in Fig. 17(c). The vertical displacement U_2 in Fig. 17(d) has large value at which large σ_{11} exists as observed in Fig. 17(a).

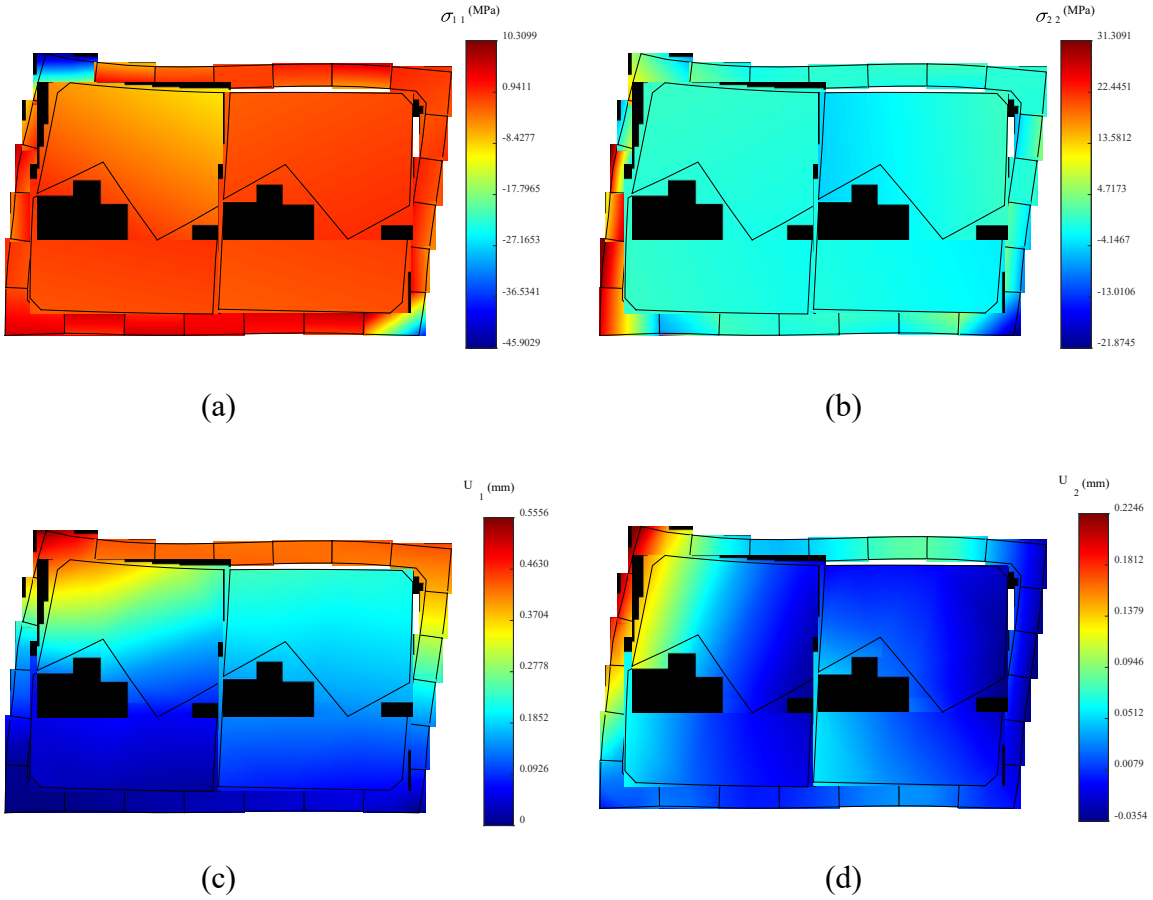

Fig. 18 Results of Example 3 with Young's modulus of infilled block 1×10^4 MPa; (a) Stress contour of σ_{11}, (b) Stress contour of σ_{22}, (c) Displacement contour of U_1, (d) Displacement contour of U_2

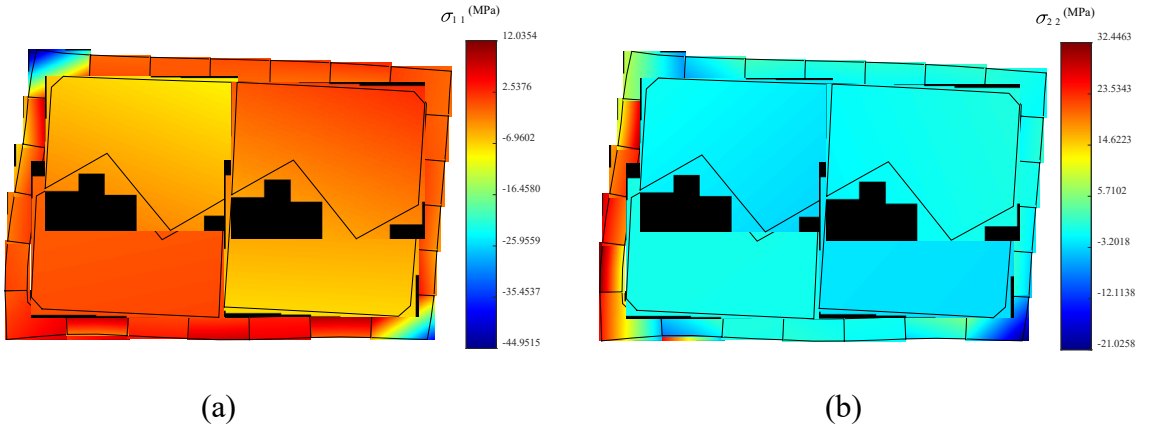

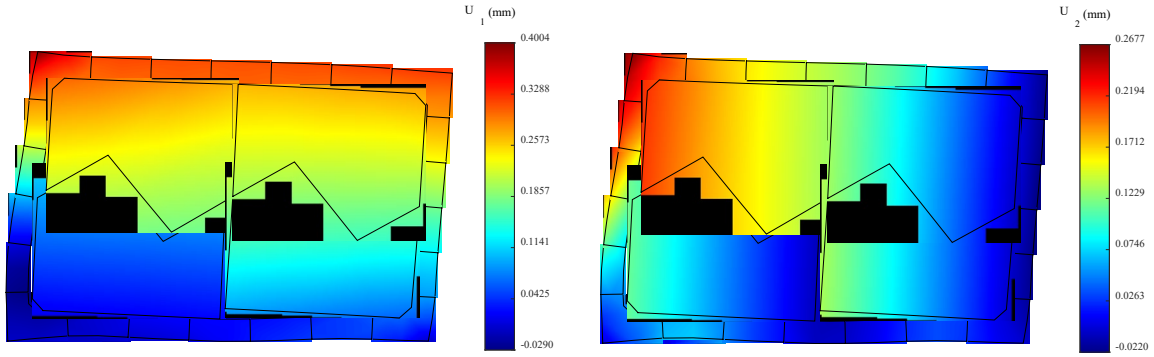

(c) (d)

Fig. 19 Results of Example 3 with Young's modulus of infilled block 5×10^4 MPa; (a) Stress contour of σ_{11}, (b) Stress contour of σ_{22}, (c) Displacement contour of U_1, (d) Displacement contour of U_2

Moreover, to further investigate the effect of stiffness of the infilled blocks on the structure, we change their Young's modulus to 1×10^4 MPa and 5×10^4 MPa, respectively, without modifying other settings, and the corresponding contours of stress and displacement are shown in Figs. 18 and 19, respectively. As shown in Fig. 18, when Young's modulus of infilled blocks is smaller than that of the frame, the infilled blocks are getting separated from the frame further compared to the deformation in Fig. 16, especially at the top-right corner of the structure. The maximum absolute displacements of U_1 and U_2 are both larger than those in Figs. 16(c) and (d), indicating that decreasing Young's modulus of infilled blocks will lead to a decrease of overall stiffness of the structure. On the other hand, comparing Figs. 19(a) and (b) to Figs. 16(a) and (b), we can see that increasing the stiffness of the infilled blocks does not reduce the overall stress level of the structure; on the contrary, the stress level of σ_{22} has increased to some extent in both tension and compression. The main reason for this result may be that because Young's modulus of the blocks is larger than that of the frame, the blocks are stiffer than the frame, and upper blocks 2 and 4 are clamped and lifted by the frame due to its larger deformation, leaving the block 1 isolated from the contact interaction among the blocks. Therefore, the deformation of left side of the frame is less restricted and tends to have large overturning deformation as shown in Fig. 19(b), leading to a higher tension in σ_{22} than that in Fig. 16(b). Consequently, the stress level of block 1 is lower than the other three blocks. The maximum absolute values of displacements U_1 and U_2 of the structure are also larger than those in Figs. 16(c) and (d), respectively, and the displacements at the contact interfaces between blocks 1 and 2 as well as 1 and 3 become discontinuous. These results imply that block 1 is not involved in the contact interactions of the other three blocks, and thus contributes a little to the overall stiffness of the structure.

The horizontal displacements at the loading point are listed in Table 1 for all the three cases with different Young's modulus of infilled blocks. Note that for all the three cases of Example 3 the horizontal force-displacement relation is linear and the deformation is very small compared to the size of the structure. Therefore, the assumption of stick condition for frictional contact and the node-to-node contact scheme using second-order VEM are reasonable for the contact analysis in this example. It should also be noted that the displacement obviously decreases as Young's modulus is increased.

Table 2 Displacement at the loading point in horizontal direction of Examples 3 and 4

Case	Example 3			Example 4
Young's modulus of infilled block (MPa)	1×10^4	3×10^4	5×10^4	3×10^4
Displacement (mm)	0.5556	0.3477	0.4004	0.3615

4.4 Example 4

The last example is to investigate a contact analysis of a rectangular frame with infilled blocks in which the geometries of the blocks are more complicated than those in Example 3. The blocks are connected by contact with convex and concave fitting joints. The geometry model and corresponding second-order VEM discretization are given in Fig. 20(a) and (b), respectively, where each of the twelve infilled blocks is simulated by one element. In the same manner as Example 3, a horizontal force F = 1000 N is applied at the top left of the structure, and Young's modulus and Poisson's ratio of the frame and infilled blocks are 3×10^4 MPa and 0.3, respectively.

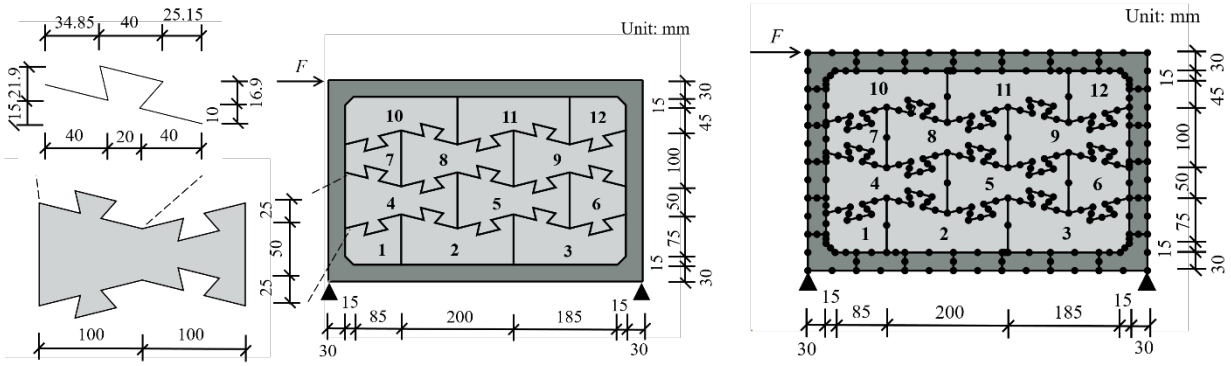

(a) (b)

Fig. 20 Model of Example 4; (a) Geometry models of rectangle frame and 12 infilled blocks, (b) Second-order VEM discretization

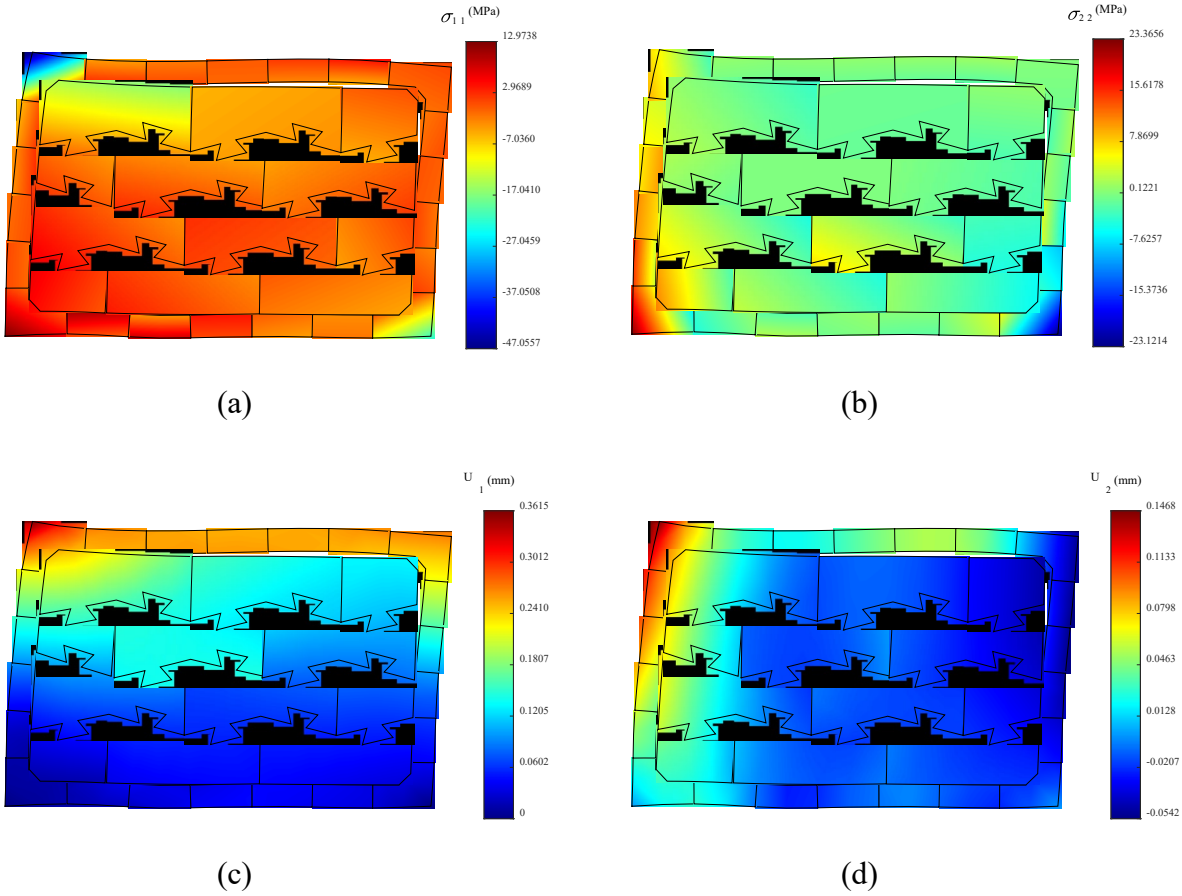

Fig. 21 Results of Example 4; (a) Stress contour of σ_{11}, (b) Stress contour of σ_{22}, (c) Displacement contour of U_1, (d) Displacement contour of U_2

The contours of stress and displacement are displayed in Figs. 21(a)-(d), and the corresponding deformations are scaled by the factor 100. Compared to the results in Figs. 16(a) and (b) of Example 3 with simpler infilled blocks, the maximum absolute values of stresses of σ_{11} in Fig. 21(a) slightly exceeds those in Fig. 16(a), while the values of σ_{22} in tension and compression become close in Fig. 21(b). On the other hand, it can be seen that the distributions of displacement in Figs. 21(c) and (d) are similar to those in Figs. 16(c) and (d), and the maximum value of U_2 in Fig. 21(d) is smaller than that in Fig. 16(d) while the maximum value of U_1 in Fig. 21(c) is larger than that in Fig. 16(c), both of which occur at the loading point. The displacement at the loading point in horizontal direction is 0.3615 mm as shown in Table 1, which is a little larger than 0.3477 mm for Example 3 with the same Young's modulus. The force-displacement relation is linear and the deformation is small also for Example 4. These results indicate that although the overall stiffness of the structure is not enhanced by the use of complicated infilled block compared to the simpler one, the lifting effect on the loading point is reduced with a smaller upward deformation. However, both types of infilled blocks in Examples 3 and 4 are effective in reducing the stress level and the displacement of the frame structure with the increase the overall stiffness of the structure by contact interactions.

5. Conclusions

In this study a second-order VEM based node-to-node scheme is proposed for 2-dimensional contact analysis. By virtue of VEM in handling arbitrary polygon element and hanging node on the element edge, the non-matching contact interface in the initial meshes can be transformed into matching one by the node insertion procedure. Then the node-to-node scheme can be constructed for normal and tangential contact analysis which are incorporated into the equilibrium equation by using Lagrange multiplier method and penalty method, respectively. Because we only consider small deformation of the structure, the tangential contact is assumed to be stick condition. Unlike the traditional node-to-segment or segment-to-segment contact which would result in larger stress deviation on non-matching contact interface if higher-order element is used, the proposed method can pass the patch test with second-order element with arbitrary polygon even concave, allowing a sparse discretization on the model without great loss of the accuracy. Calculation of the element stiffness matrix of second-order VEM uses only the values of second-order polynomials and shape functions on the element edge.

Four numerical examples including the patch test are investigated to demonstrate the effectiveness of the proposed method. In the patch test the two rectangle elastic bodies in contact are discretized by the L-shaped element with different sizes, and the contact interface is non-matching with starting meshes. The results show that analytical solution of constant stress filed can be obtained by the proposed method, showing that the proposed method is able to pass the patch test with non-convex polygon second-order element and non-matching contact interface. The second example is a contact problem of two hollow cylinders with known analytical solution, and the proposed method is investigated in three aspects: robustness with respect to small edges, computational efficiency and convergence study. It is shown that when the small edge exists on the contact interface, the displacement and stress errors are close to those obtained without small edge, while the nodal displacements become slightly oscillatory in the vicinity of the small edge. Moreover, due to the ability of capturing the nonlinear displacement field by second-order polynomial, the proposed second-order VEM is more accurate than the linear VEM with the same number of DOFs and a coarse mesh on the model, which is helpful in structural analysis with complex geometry model. Besides, a mesh refinement with decreasing average element size is used for the convergence study of the proposed method in contact problem, and the corresponding convergence study of linear elasticity problem is also implemented, where the two hollow cylinders are combined into one-piece hollow cylinder. The results show that for both contact and linear elasticity problems the order of convergence rate of displacement error is 2 as expected, and the order of convergence rate of stress is around 1, indicating that the proposed method will converge to the analytical solution in both contact and linear elasticity problems.

The third and fourth examples investigate the multi-body contact problems of rectangle frame with different types of infilled blocks under a concentrated horizontal force. Based on the discretization property of arbitrary polygon of VEM, each infilled block can be simulated by only one element even it has a complicated geometry such as jigsaw-like block in Example 4. All the non-matching contact interfaces are transferred to matching ones by repeating the node

insertion procedure. It can be seen from the results that both simple and complicated infilled blocks can significantly increase the structural stiffness by contact interaction and thus reduce the displacement and stress level of the structure. Moreover, it is interesting to note that assigning a larger Young's modulus to the infilled block does not always lead to a better result, because a too stiff infilled block results in a large stress levels of the structure. The main reason for this would be because the ability of deformation of the frame and infilled blocks are different, one or some blocks may not be in contact with other blocks and not involved in resisting against the external force, contributing little to the overall structural stiffness.

Acknowledgement

This research is partially supported by China Scholarship Council (File No. 201806050114).

Reference

1. Wriggers P (1995) Finite element algorithms for contact problems. Arch Comput Methods Eng 2:1–49. https://doi.org/10.1007/BF02736195
2. Wriggers P (2006) Computational contact mechanics, second. Springer Berlin Heidelberg
3. Aharoni L, Bachelet I, Carstensen J V. (2021) Topology optimization of rigid interlocking assemblies. Comput Struct 250:106521. https://doi.org/10.1016/j.compstruc.2021.106521
4. Lawry M, Maute K (2018) Level set shape and topology optimization of finite strain bilateral contact problems. Int J Numer Methods Eng 113:1340–1369. https://doi.org/10.1002/nme.5582
5. Niu C, Zhang W, Gao T (2020) Topology optimization of elastic contact problems with friction using efficient adjoint sensitivity analysis with load increment reduction. Comput Struct 238:106296. https://doi.org/10.1016/j.compstruc.2020.106296
6. Lin T, Ou H, Li R (2007) A finite element method for 3D static and dynamic contact/impact analysis of gear drives. Comput Methods Appl Mech Eng 196:1716–1728. https://doi.org/10.1016/j.cma.2006.09.014
7. Belytschko T, Liu WK, Moran B, Khalil i. E (2013) Nonlinear finite elements for continua and structures. John wiley & sons
8. Francavilla A, Zienkiewicz OC (1975) A note on numerical computation of elastic contact problems. Int J Numer Methods Eng 9:913–924. https://doi.org/10.1002/nme.1620090410
9. Hughes TJR, Taylor RL, Sackman JL, Curnier A, Kanoknukulchai W (1976) A finite element method for a class of contact-impact problems. Comput Methods Appl Mech Eng 8:249–276. https://doi.org/10.1016/0045-7825(76)90018-9
10. Papadopoulos P, Taylor RL (1992) A mixed formulation for the finite element solution of contact problems. Comput Methods Appl Mech Eng 94:373–389.

https://doi.org/10.1016/0045-7825(92)90061-N

11. Puso MA, Laursen TA (2004) A mortar segment-to-segment contact method for large deformation solid mechanics. Comput Methods Appl Mech Eng 193:601–629. https://doi.org/10.1016/j.cma.2003.10.010

12. Laursen TA, Puso MA, Sanders J (2012) Mortar contact formulations for deformable-deformable contact: Past contributions and new extensions for enriched and embedded interface formulations. Comput Methods Appl Mech Eng 205–208:3–15. https://doi.org/10.1016/j.cma.2010.09.006

13. Bitencourt LAG, Manzoli OL, Prazeres PGC, Rodrigues EA, Bittencourt TN (2015) A coupling technique for non-matching finite element meshes. Comput Methods Appl Mech Eng 290:19–44. https://doi.org/10.1016/j.cma.2015.02.025

14. Xing W, Song C, Tin-Loi F (2018) A scaled boundary finite element based node-to-node scheme for 2D frictional contact problems. Comput Methods Appl Mech Eng 333:114–146. https://doi.org/10.1016/j.cma.2018.01.012

15. Xing W, Zhang J, Song C, Tin-Loi F (2019) A node-to-node scheme for three-dimensional contact problems using the scaled boundary finite element method. Comput Methods Appl Mech Eng 347:928–956. https://doi.org/10.1016/j.cma.2019.01.015

16. Hussein A, Aldakheel F, Hudobivnik B, Wriggers P, Guidault PA, Allix O (2019) A computational framework for brittle crack-propagation based on efficient virtual element method. Finite Elem Anal Des 159:15–32. https://doi.org/10.1016/j.finel.2019.03.001

17. Wriggers P, Rust WT, Reddy BD (2016) A virtual element method for contact. Comput Mech 58:1039–1050. https://doi.org/10.1007/s00466-016-1331-x

18. Brezzi F, Lipnikov K, Simoncini V (2005) A family of mmetic finite difference methods on polygonal and polyhedral meshes. Math Model Methods Appl Sci 15:1533–1551

19. Beirão da Veiga L, Brezzi F, Cangiani A, Manzini G, Marini LD, Russo A (2013) Basic principles of virtual element methods. Math Model Methods Appl Sci 23:199–214. https://doi.org/10.1142/S0218202512500492

20. Gain AL, Talischi C, Paulino GH (2014) On the virtual element method for three-dimensional linear elasticity problems on arbitrary polyhedral meshes. Comput Methods Appl Mech Eng 282:132–160. https://doi.org/10.1016/j.cma.2014.05.005

21. Beirão da Veiga L, Brezzi F, Marini LD (2013) Virtual elements for linear elasticity problems. SIAM J Numer Anal 51:794–812

22. Artioli E, Beirão da Veiga L, Lovadina C, Sacco E (2017) Arbitrary order 2D virtual elements for polygonal meshes: part I, elastic problem. Comput Mech 60:355–377. https://doi.org/10.1007/s00466-017-1404-5

23. Chi H, da Veiga LB, Paulino GH (2017) Some basic formulations of the virtual element method (VEM) for finite deformations. Comput Methods Appl Mech Eng 318:148–192. https://doi.org/10.1016/j.cma.2016.12.020

24. Nguyen-Thanh VM, Zhuang X, Nguyen-Xuan H, Rabczuk T, Wriggers P (2018) A virtual rlement method for 2D linear elastic fracture analysis. Comput Methods Appl Mech Eng 340:366–395. https://doi.org/10.1016/j.cma.2018.05.021

25. Chi H, Pereira A, Menezes IFM, Paulino GH (2020) Virtual element method (VEM)-based topology optimization: an integrated framework. Struct Multidiscip Optim 62:1089–1114. https://doi.org/10.1007/s00158-019-02268-w

26. Fukushima K, Ohsaki M, Mikami T, Miyazu Y (2016) Combinatorial optimization of latticed blocks composed of various unit shapes for seismic retrofit. J Struct Constr Eng （in Japanese） 81:1657–1664

27. Kimura T, Ohsaki M, Yamaoka Y (2018) Shape and topology optimization of shear wall consisting of latticed blocks. In: Proc. IASS Symposium 2018, Boston, USA. Int. Assoc. Shell and Spatial Struct, Paper No. 234, 2018

28. Bulleit WM, Sandberg LB, Drewek MW, O'Bryant TL (1999) Behavior and modeling of wood-pegged timber frames. J Struct Eng 125:3–9

29. Beirão da Veiga L, Brezzi F, Marini LD, Russo A (2014) The Hitchhiker's guide to the virtual element method. Math Model Methods Appl Sci 24:1541–1573. https://doi.org/10.1142/S021820251440003X

30. Mengolini M, Benedetto MF, Aragón AM (2019) An engineering perspective to the virtual element method and its interplay with the standard finite element method. Comput Methods Appl Mech Eng 350:995–1023. https://doi.org/10.1016/j.cma.2019.02.043

31. (2018) MATLAB. Natick, Massachusetts: The MathWorks Inc

32. El-Abbasi N, Bathe KJ (2001) Stability and patch test performance of contact discretizations and a new solution algorithm. In: Comput. Struct.

33. Da Veiga LB, Lovadina C, Russo A (2017) Stability analysis for the virtual element method. Math Model Methods Appl Sci 27:2557–2594. https://doi.org/10.1142/S021820251750052X

34. Brenner SC, Sung LY (2018) Virtual element methods on meshes with small edges or faces

35. Beirão da Veiga L, Dassi F, Russo A (2017) High-order Virtual Element Method on polyhedral meshes. Comput Math with Appl 74:1110–1122. https://doi.org/10.1016/j.camwa.2017.03.021

Appendix

Suppose element K has n vertices denoted as $\boldsymbol{x}_i = [x_i, y_i]$ $(i = 1, 2, \ldots, n)$. The non-dimensional values ξ and η are obtained by scaling x and y, respectively, by the diameter h^K of element K as [29]

$$\xi = \frac{x-\overline{x}}{h^K},\ \eta = \frac{y-\overline{y}}{h^K} \tag{A1}$$

where $\overline{x}$ and $\overline{y}$ are the coordinates of the centroid of element calculated as $[\overline{x},\overline{y}] = \frac{1}{n}\sum_{i=1}^{n} \boldsymbol{x}_i$. The vector-valued basis functions of local virtual element space $V_h \times V_h$ and second-order polynomial space $P^2 \times P^2$ are given as

$$\begin{bmatrix} \varphi_1 & 0 & \varphi_2 & 0 & \dots & \varphi_{2n+1} & 0 \\ 0 & \varphi_1 & 0 & \varphi_2 & \dots & 0 & \varphi_{2n+1} \end{bmatrix} = \begin{bmatrix} \boldsymbol{\varphi}_1 & \boldsymbol{\varphi}_2 & \boldsymbol{\varphi}_3 & \boldsymbol{\varphi}_4 & \dots & \boldsymbol{\varphi}_{4n+1} & \boldsymbol{\varphi}_{4n+2} \end{bmatrix} \tag{A2}$$

$$\begin{bmatrix} 1 & 0 & \eta & \xi & 0 & \eta & \xi^2 & 0 & \eta^2 & 0 & \xi\eta & 0 \\ \underbrace{0}_{\boldsymbol{p}_1} & \underbrace{1}_{\boldsymbol{p}_2} & \underbrace{-\xi}_{\boldsymbol{p}_3} & \underbrace{0}_{\boldsymbol{p}_4} & \underbrace{\eta}_{\boldsymbol{p}_5} & \underbrace{\xi}_{\boldsymbol{p}_6} & \underbrace{0}_{\boldsymbol{p}_7} & \underbrace{\xi^2}_{\boldsymbol{p}_8} & \underbrace{0}_{\boldsymbol{p}_9} & \underbrace{\eta^2}_{\boldsymbol{p}_{10}} & \underbrace{0}_{\boldsymbol{p}_{11}} & \underbrace{\xi\eta}_{\boldsymbol{p}_{12}} \end{bmatrix} \tag{A3}$$

respectively, where $\boldsymbol{\varphi}_{2i-1} = [\varphi_i \quad 0]$, $\boldsymbol{\varphi}_{2i} = [0 \quad \varphi_i]$ $(i = 1,2,\dots,2n+1)$ and $\boldsymbol{p}_1$-$\boldsymbol{p}_{12}$ represent the 12 basis functions of $P^2 \times P^2$ as discussed in Sec. 2.2. The basis functions in (A2) and (A3) will be used in the following sections to derive the matrix implementation of second order VEM.

A1 Calculation of matrix *G* and projector $\boldsymbol{\Pi}$

Based on the orthogonality condition Eq. (10), we first replace $\boldsymbol{v}_h$ by $\boldsymbol{\varphi}_i, i = 1,2,\dots,4n+2$ and use the linearity of a^K to obtain

$$a^E\left(\boldsymbol{p}_\alpha, \Pi^\nabla \boldsymbol{\varphi}_i\right) = a^E\left(\boldsymbol{p}_\alpha, \boldsymbol{\varphi}_i\right) \quad \text{for } \alpha = 1,2,\dots,12, \forall \boldsymbol{p}_\alpha \in P_2 \times P_2 \tag{A4}$$

By expressing $\Pi^\nabla \boldsymbol{\varphi}_i = \sum_{\beta=1}^{12} S_{i,\beta}\boldsymbol{p}_\beta,\ \boldsymbol{p}_\beta \in P^2 \times P^2$, the matrix form of Eq. (A4) is given as

$$\begin{bmatrix} a^K(\boldsymbol{p}_1,\boldsymbol{p}_1) & a^K(\boldsymbol{p}_1,\boldsymbol{p}_2) & \dots & a^K(\boldsymbol{p}_1,\boldsymbol{p}_{12}) \\ a^K(\boldsymbol{p}_2,\boldsymbol{p}_1) & a^K(\boldsymbol{p}_2,\boldsymbol{p}_2) & \dots & a^K(\boldsymbol{p}_2,\boldsymbol{p}_{12}) \\ \vdots & \vdots & \ddots & \vdots \\ a^K(\boldsymbol{p}_{12},\boldsymbol{p}_1) & a^K(\boldsymbol{p}_{12},\boldsymbol{p}_2) & \dots & a^K(\boldsymbol{p}_{12},\boldsymbol{p}_{12}) \end{bmatrix} \begin{bmatrix} S_{i,1} \\ S_{i,2} \\ \vdots \\ S_{i,12} \end{bmatrix} = \begin{bmatrix} a^K(\boldsymbol{p}_1,\boldsymbol{\varphi}_i) \\ a^K(\boldsymbol{p}_2,\boldsymbol{\varphi}_i) \\ \vdots \\ a^K(\boldsymbol{p}_{12},\boldsymbol{\varphi}_i) \end{bmatrix} \Rightarrow \boldsymbol{G}\boldsymbol{\Pi}_i = \boldsymbol{B}_i \tag{A5}$$

where $\boldsymbol{\Pi}_i = \left[S_{i,1}, S_{i,2}, \dots, S_{i,12}\right]^T$ is the *i*th column of the matrix representation $\boldsymbol{\Pi}$ of projector Π^∇ and $\boldsymbol{B}_i = \left[a^K(\boldsymbol{p}_1,\boldsymbol{\varphi}_i), a^K(\boldsymbol{p}_2,\boldsymbol{\varphi}_i), \dots, a^K(\boldsymbol{p}_{12},\boldsymbol{\varphi}_i)\right]$; Matrix $\boldsymbol{G}$ is defined as the same as in Eq. (12) . Repeat Eq. (A4) for all the $4n$+2 basis functions $\boldsymbol{\varphi}_i$ we can obtain

$$\boldsymbol{G}\left[\boldsymbol{\Pi}_1 \quad \boldsymbol{\Pi}_2 \quad \dots \quad \boldsymbol{\Pi}_{4n+1} \quad \boldsymbol{\Pi}_{4n+2}\right] = \left[\boldsymbol{B}_1 \quad \boldsymbol{B}_2 \quad \dots \quad \boldsymbol{B}_{4n+1} \quad \boldsymbol{B}_{4n+2}\right] \Rightarrow \boldsymbol{G}\boldsymbol{\Pi} = \boldsymbol{B} \tag{A6}$$

where $\boldsymbol{\Pi} = \begin{bmatrix} \boldsymbol{\Pi}_1 & \boldsymbol{\Pi}_2 & \dots & \boldsymbol{\Pi}_{4n+1} & \boldsymbol{\Pi}_{4n+2} \end{bmatrix}$ and $\boldsymbol{B} = \begin{bmatrix} \boldsymbol{B}_1 & \boldsymbol{B}_2 & \dots & \boldsymbol{B}_{4n+1} & \boldsymbol{B}_{4n+2} \end{bmatrix}$.

Next we calculate the entries of matrix $\boldsymbol{G}$ and $\boldsymbol{B}$ in detail. According to the definition of bilinear form a^K in Eq. (2) and divergence theorem, we have

$$\begin{aligned} \boldsymbol{G}_{\alpha\beta} &= a^K\left(\boldsymbol{p}_\alpha, \boldsymbol{p}_\beta\right) = \int_{\Omega^K} \boldsymbol{\sigma}\left(\boldsymbol{p}_\alpha\right) : \boldsymbol{\varepsilon}\left(\boldsymbol{p}_\beta\right) d\Omega^K \\ &= \int_{\partial\Omega^K} \mathbb{C}\boldsymbol{\varepsilon}\left(\boldsymbol{p}_\alpha\right)\mathbf{n}_{\partial\Omega^K} \cdot \boldsymbol{p}_\beta d\Gamma - \int_{\Omega^K} \boldsymbol{p}_\beta \cdot \left[\nabla \cdot \left(\mathbb{C}\boldsymbol{\varepsilon}\left(\boldsymbol{p}_\alpha\right)\right)\right] d\Omega^K, \ \alpha, \beta = 1, 2, \dots, 12 \end{aligned} \tag{A7}$$

$$\begin{aligned} \boldsymbol{B}_{\alpha i} &= a^K\left(\boldsymbol{p}_\alpha, \boldsymbol{\varphi}_i\right) = \int_{\Omega^K} \boldsymbol{\sigma}\left(\boldsymbol{p}_\alpha\right) : \boldsymbol{\varepsilon}\left(\boldsymbol{\varphi}_i\right) d\Omega^K \\ &= \int_{\partial\Omega^K} \mathbb{C}\boldsymbol{\varepsilon}\left(\boldsymbol{p}_\alpha\right)\mathbf{n}_{\partial\Omega^K} \cdot \boldsymbol{\varphi}_i d\Gamma - \int_{\Omega^K} \boldsymbol{\varphi}_i \cdot \left[\nabla \cdot \left(\mathbb{C}\boldsymbol{\varepsilon}\left(\boldsymbol{p}_\alpha\right)\right)\right] d\Omega^K, \ \alpha = 1, 2, \dots, 12; i = 1, 2, \dots, 4n+2 \end{aligned} \tag{A8}$$

where $\mathbf{n}_{\partial\Omega^K}$ is the unit outward normal vector to the element boundary $\partial\Omega^K$, and $\nabla\cdot$ is the divergence operator. It can be seen from Eqs. (A7) and (A8) that to obtain matrices $\boldsymbol{G}$ and $\boldsymbol{B}$ we have to calculate the following four integrals:

(I1) $\int_{\partial\Omega^K} \mathbb{C}\boldsymbol{\varepsilon}\left(\boldsymbol{p}_\alpha\right)\mathbf{n}_{\partial\Omega^K} \cdot \boldsymbol{p}_\beta d\Gamma$ in Eq. (A7)

Because $\boldsymbol{p}_\alpha$ and $\boldsymbol{p}_\beta$ are explicitly known as in Eq. (A3) and $\mathbf{n}_{\partial\Omega^K}$ is piece-wise constant vector along the boundary of polygon element K, integral (I1) can be easily calculated using Gauss-Lobatto quadrature rule on each edge of element K

$$\begin{aligned} &\int_{\partial\Omega^K} \mathbb{C}\boldsymbol{\varepsilon}\left(\boldsymbol{p}_\alpha\right)\mathbf{n}_{\partial\Omega^K} \cdot \boldsymbol{p}_\beta d\Gamma = \sum_{j=1}^{n} \int_{\partial\Omega_j^K} \mathbb{C}\boldsymbol{\varepsilon}\left(\boldsymbol{p}_\alpha\right)\mathbf{n}_{\partial\Omega_j^K} \cdot \boldsymbol{p}_\beta d\Gamma \\ &= \sum_{j=1}^{n} \frac{\left|\partial\Omega_j^K\right|}{2} \sum_{r=1}^{3} w_r \mathbb{C}\boldsymbol{\varepsilon}\left(\boldsymbol{p}_\alpha\big|_{\boldsymbol{\theta}_r}\right)\mathbf{n}_{\partial\Omega^K} \cdot \boldsymbol{p}_\beta\big|_{\boldsymbol{\theta}_r}, \ \alpha, \beta = 1, 2, \dots, 12 \end{aligned} \tag{A9}$$

where $\partial\Omega_j^K$ represent the jth ($j = 1, 2, \dots, n$) edge of element K and $\mathbf{n}_{\partial\Omega_j^K}$ is the corresponding unit outward normal vector, and $\left|\partial\Omega_j^K\right|$ is the length of $\partial\Omega_j^K$; $\boldsymbol{\theta}_r$ and w_r (r=1,2,3) are the Gauss-Lobatto points and the associated weights for calculating the integration over each edge $\partial\Omega_j^K$. Recall that since the order of $\boldsymbol{p}_\alpha$ and $\boldsymbol{p}_\beta$ are up to 2, the three point Gauss-Lobatto quadrature rule is able to obtain the exact result of integral $\int_{\partial\Omega_j^K} \mathbb{C}\boldsymbol{\varepsilon}\left(\boldsymbol{p}_\alpha\right)\mathbf{n}_{\partial\Omega_j^K} \cdot \boldsymbol{p}_\beta d\Gamma$ [30].

(I2) $\int_{\Omega^K} \boldsymbol{p}_\beta \cdot \left[\nabla \cdot \left(\mathbb{C}\boldsymbol{\varepsilon}\left(\boldsymbol{p}_\alpha\right)\right)\right] d\Omega^K$ in Eq. (A7)

It can be observed from Eq. (A3) that when $\alpha \le 6$ the integral (I2) vanish due to the twice differential of $\boldsymbol{p}_\alpha$. For $\alpha > 6$, the result of $\boldsymbol{p}_\beta \cdot \left[\nabla \cdot \left(\mathbb{C}\boldsymbol{\varepsilon}\left(\boldsymbol{p}_\alpha\right)\right)\right]$ is a polynomial with explicit form

$$\boldsymbol{p}_\beta \cdot \left[\nabla \cdot \left(\mathbb{C}\boldsymbol{\varepsilon}\left(\boldsymbol{p}_\alpha\right)\right)\right] = \sum_{m_1,m_2=0}^{d} c_{m_1 m_2} \xi^{m_1} \eta^{m_2} = p_{\alpha\beta}^{d},\ \alpha = 7,8,\cdots,12; \beta = 1,2,\ldots,12 \tag{A10}$$

where d is the highest order of $\boldsymbol{p}_\beta \cdot \left[\nabla \cdot \left(\mathbb{C}\boldsymbol{\varepsilon}\left(\boldsymbol{p}_\alpha\right)\right)\right]$ which can be easily obtained from the orders of $\boldsymbol{p}_\alpha$ and $\boldsymbol{p}_\beta$. Integration (I2) can be now calculated using divergence theorem as

$$\begin{aligned} &\int_{\Omega^K} \boldsymbol{p}_\beta \cdot \left[\nabla \cdot \left(\mathbb{C}\boldsymbol{\varepsilon}\left(\boldsymbol{p}_\alpha\right)\right)\right] d\Omega^K = \int_{\Omega^K} p_{\alpha\beta}^{d} d\Omega^K = \int_{\Omega^K} \nabla \cdot \begin{pmatrix} p_{\alpha\beta}^{d+1} \\ 0 \end{pmatrix} d\Omega^K \\ &= = \int_{\partial\Omega^K} \begin{pmatrix} p_{\alpha\beta}^{d+1} \\ 0 \end{pmatrix}^T \mathbf{n}_{\partial\Omega^K} d\Gamma,\ \alpha = 7,8,\ldots,12; \beta = 1,2,\ldots,12 \end{aligned} \tag{A11}$$

with $p_{\alpha\beta}^{d+1} = \sum_{m_1,m_2=0}^{d} c_{m_1 m_2} \frac{\xi^{m_1+1}}{m_1+1} \eta^{m_2}$. In this way the integral (I2) over the element domain Ω^K is transformed into the integral on the element boundary $\partial\Omega^K$, and Eq. (A11) can be calculated using Gaussian-Lobatto quadrature rule as in integral (I1)

(I3) $\int_{\partial\Omega^K} \mathbb{C}\boldsymbol{\varepsilon}\left(\boldsymbol{p}_\alpha\right) \mathbf{n}_{\partial\Omega^K} \cdot \boldsymbol{\varphi}_i d\Gamma$ in Eq. (A8)

Similar to Eq. (A9), integral (I3) can be calculated as follows

$$\begin{aligned} &\int_{\partial\Omega^K} \mathbb{C}\boldsymbol{\varepsilon}\left(\boldsymbol{p}_\alpha\right) \mathbf{n}_{\partial\Omega^K} \cdot \boldsymbol{\varphi}_i d\Gamma = \sum_{j=1}^{n} \int_{\partial\Omega_j^K} \mathbb{C}\boldsymbol{\varepsilon}\left(\boldsymbol{p}_\alpha\right) \mathbf{n}_{\partial\Omega_j^K} \cdot \boldsymbol{\varphi}_i d\Gamma \\ &= \sum_{j=1}^{n} \frac{\left|\partial\Omega_j^K\right|}{2} \sum_{r=1}^{3} w_r \mathbb{C}\boldsymbol{\varepsilon}\left(\boldsymbol{p}_\alpha\big|_{\theta_r}\right) \mathbf{n}_{\partial\Omega^K} \cdot \boldsymbol{\varphi}_i\big|_{\theta_r},\ \alpha = 1,2,\ldots,12; i = 1,2,\ldots,4n+2 \end{aligned} \tag{A12}$$

As discussed in Sec. 2.2, because the basis function $\boldsymbol{\varphi}_i$ is a second order polynomial on the element edge and satisfies the Kronecker-delta property, and the Gaussian-Lobatto points at each element edge are exactly the points where DOF of type (i) and (ii) are defined, $\boldsymbol{\varphi}_i\big|_{\theta_r}$ is computable for all the basis functions and is 0 for the basis functions associated with DOF of type (iii).

(I4) $\int_{\Omega^K} \boldsymbol{\varphi}_i \cdot \left[\nabla \cdot \left(\mathbb{C}\boldsymbol{\varepsilon}\left(\boldsymbol{p}_\alpha\right)\right)\right] d\Omega^K$ in Eq. (A8)

Likewise, Integral (I4) is only non-zero for $\alpha > 6$. Since the order of $\boldsymbol{p}_\alpha$ is no greater than 2, the term $\nabla \cdot \left(\mathbb{C}\boldsymbol{\varepsilon}\left(\boldsymbol{p}_\alpha\right)\right)$ can be decomposed to the linear combination of vectors $\boldsymbol{p}_1 = [1,0]^T$ and $\boldsymbol{p}_2 = [0,1]^T$ due to the twice differential of $\boldsymbol{p}_\alpha$, which can be written as

$$\nabla \cdot \left(\mathbb{C}\boldsymbol{\varepsilon}\left(\boldsymbol{p}_\alpha\right)\right) = d_{\alpha,1} \begin{bmatrix} 1 \\ 0 \end{bmatrix} + d_{\alpha,2} \begin{bmatrix} 0 \\ 1 \end{bmatrix}, \alpha = 7,8,\ldots,12 \tag{A13}$$

where $d_{\alpha,1}$ and $d_{\alpha,2}$ are the two known constants obtained with different $\boldsymbol{p}_\alpha, \alpha = 7,8,\ldots,12$. Then the integral (I4) can be reformulated

$$\int_{\Omega^K} \boldsymbol{\varphi}_i \cdot \left[\nabla \cdot \left(\mathbb{C}\boldsymbol{\varepsilon}\left(\boldsymbol{p}_\alpha\right)\right)\right] d\Omega^K = \sum_{c=1}^{2} d_{\alpha,c} \int_{\Omega^K} \boldsymbol{\varphi}_i \cdot \boldsymbol{p}_c d\Omega^K, \ \alpha = 7,8,\ldots,12; i = 1,2,\ldots,4n+2 \tag{A14}$$

Since the basis function $\boldsymbol{\varphi}_i$, $i = 1,2,\ldots,4n+2$ satisfies the Kronecker-delta property and recall the definitions of DOF for type (i), (ii) and (iii) as given in Sec. 2.2, Eq. (A14) is only non-zero for the basis functions $\boldsymbol{\varphi}_{4n+1}$ and $\boldsymbol{\varphi}_{4n+2}$. Therefore, calculation of Eq. (A14) can be given as

$$\int_{\Omega^K} \boldsymbol{\varphi}_i \cdot \left[\nabla \cdot \left(\mathbb{C}\boldsymbol{\varepsilon}\left(\boldsymbol{p}_\alpha\right)\right)\right] d\Omega^K = \begin{cases} \left|\Omega^K\right| d_{\alpha,c} & \text{if } i = 4n+c \\ 0 & \text{else} \end{cases}, \ \alpha = 7,8,\cdots,12; i = 1,2,\ldots,4n+2 \tag{A15}$$

However, as can be seen from Eqs. (A3), (A7) and (A8) that the first three rows of matrices $\boldsymbol{G}$ and $\boldsymbol{B}$ are always equal to 0 because $\boldsymbol{p}_1, \boldsymbol{p}_2, \boldsymbol{p}_3$ represent the rigid body motion and thus have no contribution to the strain energy [30]. Therefore, three additional equations should be added to replace the first three rows of matrices $\boldsymbol{G}$ and $\boldsymbol{B}$ to avoid rank deficiency. According to Ref. [30], the following Euclidean scalar product on the $2n$ DOF of type (i) is used for the replacement

$$\frac{1}{n}\sum_{j=1}^{2n} \mathrm{dof}_j\left(\Pi^{\nabla}\boldsymbol{\varphi}_i\right)\mathrm{dof}_j\left(\boldsymbol{p}_\alpha\right) = \frac{1}{n}\sum_{j=1}^{2n} \mathrm{dof}_j\left(\boldsymbol{\varphi}_i\right)\mathrm{dof}_j\left(\boldsymbol{p}_\alpha\right), \ \alpha = 1,2,3 \tag{A16}$$

More specifically, the left-hand side of Eq. (A16) can be written in a matrix form as

$$\begin{aligned} &\frac{1}{n}\sum_{j=1}^{2n} \mathrm{dof}_j\left(\Pi^{\nabla}\boldsymbol{\varphi}_i\right)\mathrm{dof}_j\left(\boldsymbol{p}_\alpha\right) = \frac{1}{n}\sum_{j=1}^{2n} \mathrm{dof}_j\left(\sum_{\beta=1}^{12}\left(S_{i,\beta}\boldsymbol{p}_\beta\right)\right)\mathrm{dof}_j\left(\boldsymbol{p}_\alpha\right) \\ &= \left[\frac{1}{n}\sum_{j=1}^{2n} \mathrm{dof}_j\left(\boldsymbol{p}_1\right)\mathrm{dof}_j\left(\boldsymbol{p}_\alpha\right) \quad \frac{1}{n}\sum_{j=1}^{2n} \mathrm{dof}_j\left(\boldsymbol{p}_2\right)\mathrm{dof}_j\left(\boldsymbol{p}_\alpha\right) \quad \cdots \quad \frac{1}{n}\sum_{j=1}^{2n} \mathrm{dof}_j\left(\boldsymbol{p}_{12}\right)\mathrm{dof}_j\left(\boldsymbol{p}_\alpha\right)\right] \begin{bmatrix} S_{i,1} \\ S_{i,2} \\ \vdots \\ S_{i,12} \end{bmatrix} \\ &= \tilde{\boldsymbol{G}}_\alpha \boldsymbol{\Pi}_i, \ \alpha = 1,2,3 \end{aligned} \tag{A17}$$

By denoting the right-hand side as $\frac{1}{n}\sum_{j=1}^{2n} \mathrm{dof}_j\left(\boldsymbol{\varphi}_i\right)\mathrm{dof}_j\left(\boldsymbol{p}_\alpha\right) = \tilde{B}_{i,\alpha}, \ \alpha = 1,2,3$, Eq. (A16) can be reformulated as follows to match the form of Eq. (A6)

$$\begin{aligned} &\frac{1}{n}\sum_{j=1}^{2n} \mathrm{dof}_j\left(\Pi^{\nabla}\boldsymbol{\varphi}_i\right)\mathrm{dof}_j\left(\boldsymbol{p}_\alpha\right) = \frac{1}{n}\sum_{j=1}^{2n} \mathrm{dof}_j\left(\boldsymbol{\varphi}_i\right)\mathrm{dof}_j\left(\boldsymbol{p}_\alpha\right), \ \alpha = 1,2,3 \\ &\Rightarrow \begin{bmatrix} \tilde{\boldsymbol{G}}_1 \\ \tilde{\boldsymbol{G}}_2 \\ \tilde{\boldsymbol{G}}_3 \end{bmatrix} \boldsymbol{\Pi}_i = \begin{bmatrix} \tilde{B}_{i,1} \\ \tilde{B}_{i,2} \\ \tilde{B}_{i,3} \end{bmatrix} \Rightarrow \tilde{\boldsymbol{G}}\boldsymbol{\Pi}_i = \tilde{\boldsymbol{B}}_i \end{aligned} \tag{A18}$$

Extend Eq. (A18) for all the basis functions $\boldsymbol{\varphi}_i, i=1,2,\ldots,4n+2$ we will have

$$\tilde{\boldsymbol{G}}\left[\boldsymbol{\Pi}_1 \quad \boldsymbol{\Pi}_2 \quad \ldots \quad \boldsymbol{\Pi}_{4n+2}\right]=\left[\tilde{\boldsymbol{B}}_1 \quad \tilde{\boldsymbol{B}}_2 \quad \ldots \quad \tilde{\boldsymbol{B}}_{4n+2}\right] \Rightarrow \tilde{\boldsymbol{G}}\boldsymbol{\Pi}=\tilde{\boldsymbol{B}} \tag{A19}$$

Note that in Eqs. (A16)–(A19) only the $2n$ DOFs of type (i) are used. Replacing the first three rows of matrices $\boldsymbol{G}$ and $\boldsymbol{B}$ in Eq. (A6) by Eq. (A19) yields

$$\begin{bmatrix} \tilde{\boldsymbol{G}} \\ \boldsymbol{G}_4 \\ \boldsymbol{G}_5 \\ \vdots \\ \boldsymbol{G}_{12} \end{bmatrix} \boldsymbol{\Pi}=\begin{bmatrix} \tilde{\boldsymbol{B}} \\ \boldsymbol{B}_4 \\ \boldsymbol{B}_5 \\ \vdots \\ \boldsymbol{B}_{12} \end{bmatrix} \Rightarrow \tilde{\boldsymbol{G}}_c\boldsymbol{\Pi}=\tilde{\boldsymbol{B}}_c \tag{A20}$$

where $\boldsymbol{G}_\alpha$ and $\boldsymbol{B}_\alpha$ $(\alpha=4,5,\ldots,12)$ represent the αth row of $\boldsymbol{G}$ and $\boldsymbol{B}$, respectively. Based on Eq. (A20) the matrix representation $\boldsymbol{\Pi}$ of projector $\prod^{\nabla}$ can be calculated by $\boldsymbol{\Pi}=\tilde{\boldsymbol{G}}_c^{-1}\tilde{\boldsymbol{B}}_c$, and the component of consistency part in Eq. (12) can be finally obtained by

$$\left(\boldsymbol{k}_c^K\right)_{ij}=\left(\boldsymbol{\Pi}^T\boldsymbol{G}\boldsymbol{\Pi}\right)_{ij}=\left(\left(\tilde{\boldsymbol{G}}_c^{-1}\tilde{\boldsymbol{B}}_c\right)^T\boldsymbol{G}\left(\tilde{\boldsymbol{G}}_c^{-1}\tilde{\boldsymbol{B}}_c\right)\right)_{ij}, \text{for } i,j=1,2,\ldots,4n+2 \tag{A21}$$

A2 Calculation of matrix $\boldsymbol{D}$ and projector $\bar{\boldsymbol{\Pi}}$

Based on Eq. (13), matrix $\boldsymbol{D}$ is written in a form of

$$\boldsymbol{D}=\begin{bmatrix} \mathrm{dof}_1(\boldsymbol{p}_1) & \mathrm{dof}_1(\boldsymbol{p}_2) & \ldots & \mathrm{dof}_1(\boldsymbol{p}_{12}) \\ \mathrm{dof}_2(\boldsymbol{p}_1) & \mathrm{dof}_2(\boldsymbol{p}_2) & \ldots & \mathrm{dof}_2(\boldsymbol{p}_{12}) \\ \vdots & \vdots & \ddots & \vdots \\ \mathrm{dof}_{4n+2}(\boldsymbol{p}_1) & \mathrm{dof}_{4n+2}(\boldsymbol{p}_2) & \ldots & \mathrm{dof}_{4n+2}(\boldsymbol{p}_{12}) \end{bmatrix} \tag{A22}$$

and the calculation of each component in Eq. (A22) is given as follows

(1) If $j\le 4n$, the value of $\mathrm{dof}_j(\boldsymbol{p}_\beta)$ for $\beta=1,2,\ldots,12$ is the value of $\boldsymbol{p}_\beta$ on the node (including vertexes and midpoint of each edge) with the associated jth DOF.

(2) If $j>4n$, the value of $\mathrm{dof}_j(\boldsymbol{p}_\beta)$ for $\beta=1,2,\ldots,12$ is calculated according to the definition of DOF of type (iii) as follows

$$\mathrm{dof}_{4n+1}(\boldsymbol{p}_\beta)=\frac{1}{\left|\Omega^K\right|}\int_{\Omega^K}\boldsymbol{p}_\beta\cdot\begin{bmatrix}1\\0\end{bmatrix}d\Omega^K;\ \mathrm{dof}_{4n+2}(\boldsymbol{p}_\beta)=\frac{1}{\left|\Omega^K\right|}\int_{\Omega^K}\boldsymbol{p}_\beta\cdot\begin{bmatrix}0\\1\end{bmatrix}d\Omega^K \tag{A23}$$

which can be obtained by transforming into the integral on the element edge as did in Eqs. (A10) and (A11) for integral (I2). After obtaining matrix $\boldsymbol{D}$, the matrix representation $\bar{\boldsymbol{\Pi}}$ of projection $\bar{\Pi}^{\nabla}$ is calculated as $\bar{\boldsymbol{\Pi}} = \boldsymbol{D}\boldsymbol{\Pi}$ according to Eq. (14).